

NASA Technical Paper 1764

**In-Flight Boundary-Layer  
Measurements on a Hollow Cylinder  
at a Mach Number of 3.0**

Robert D. Quinn and Leslie Gong

NOVEMBER 1980



NASA Technical Paper 1764

In-Flight Boundary-Layer  
Measurements on a Hollow Cylinder  
at a Mach Number of 3.0

Robert D. Quinn and Leslie Gong  
*Dryden Flight Research Center*  
*Edwards, California*



National Aeronautics  
and Space Administration

**Scientific and Technical  
Information Branch**

1980

# IN-FLIGHT BOUNDARY-LAYER MEASUREMENTS ON A HOLLOW CYLINDER AT A MACH NUMBER OF 3.0

Robert D. Quinn and Leslie Gong  
Dryden Flight Research Center

## INTRODUCTION

The accurate calculation of turbulent skin friction and heat transfer is necessary for the efficient and safe design of high speed aircraft. There are many empirical and semiempirical theories for the prediction of skin friction and heat transfer. However, the values predicted by the various theories usually differ substantially; therefore, experiments must be performed to validate the predictions. Many skin friction and heat transfer experiments have been made in the wind tunnel (refs. 1 and 2). Unfortunately, the wind tunnel tests have had conflicting results (refs. 1, 3, and 4). Further, the data obtained from flight tests have differed from the wind tunnel results (refs. 5 and 6). This lack of agreement in results obtained from the various experimental tests has hampered the evaluation of the turbulent boundary-layer theories and clearly indicates the need for further study.

The YF-12A airplane, with its Mach 3 cruise capability, offered an excellent test-bed for compressible turbulent boundary-layer measurements. Consequently, an instrumented hollow cylinder 3.04 meters in length was installed beneath the fuselage of the YF-12A airplane to obtain flight-measured turbulent boundary-layer data that could be used to evaluate the various prediction methods. The hollow cylinder was designed to be small enough to permit it to be tested with the same instrumentation in a wind tunnel so that the flight and wind tunnel measurements could be directly compared.

This paper presents the skin friction, heat transfer, and boundary-layer profile data that were acquired on the external surface of the lower centerline of the hollow cylinder during three YF-12A flights. The data were obtained at a local Mach number of approximately 2.9, wall-to-recovery temperature ratios of 0.66 to 0.91, and a local Reynolds number of approximately  $4.3 \times 10^6$  per meter. The measurements are compared with values derived from several theoretical calculations. In addition, some boundary-layer transition data in the form of temperatures and heat transfer are presented.

## SYMBOLS

$A$	area of skin friction gage floating element, $0.694 \text{ cm}^2$
$a, b, c$	constants (eq. (2))
$C_f$	local skin friction coefficient
$C_{p,w}$	specific heat of skin material, J/kg-K
$d$	pitot-pressure probe diameter, cm
$F$	shear force, N
$F_c$	transformation function for skin friction, $\frac{\overline{C_f}}{C_f}$
$F_x$	transformation function for length Reynolds number, $\frac{N_{Re_x}}{N_{Re_x}}$ or $\frac{N_{Re_L}}{N_{Re_L}}$
$H$	enthalpy, J/kg
$h$	altitude, m
$h_H$	local heat transfer coefficient based on enthalpy, $\text{kg/m}^2\text{-sec}$
$K$	radiation geometry factor, 1.0
$L$	length of turbulent flow, m
$M$	Mach number
$N_{Re}$	unit Reynolds number, $\frac{\rho U}{\mu}$ , per m
$N_{Re_L}$	Reynolds number based on length of turbulent boundary-layer flow, $\frac{\rho_\delta U_\delta L}{\mu_\delta}$
$N_{Re_x}$	Reynolds number based on distance from cylinder leading edge, $\frac{\rho_\delta U_\delta x}{\mu_\delta}$

$N_{Re_\theta}$	Reynolds number based on momentum thickness, $\frac{\rho_\delta U_\delta \theta}{\mu_\delta}$
$p$	static pressure, N/m <sup>2</sup>
$R$	gas constant for air, 287 m <sup>2</sup> /sec <sup>2</sup> -K
$r$	radius of cylinder, cm
$St$	local Stanton number, $\frac{h_H}{\rho_\delta U_\delta}$
$s$	Reynolds analogy factor
$T$	temperature, K
$t$	time, sec
$U$	velocity, m/sec
$U_\tau$	friction velocity, $\sqrt{\frac{\tau}{\rho}}$
$x$	distance from cylinder leading edge, m
$y$	distance normal to surface of cylinder, cm
$\alpha$	angle of attack, deg
$\beta$	angle of sideslip, deg
$\gamma$	ratio of specific heats, 1.4
$\Delta p_\alpha$	differential static pressure measured by the conical probe flow direction sensor to determine cylinder angle of attack, N/m <sup>2</sup>
$\Delta p_\beta$	differential static pressure measured by the conical probe flow direction sensor to determine cylinder angle of sideslip, N/m <sup>2</sup>
$\delta$	total boundary-layer thickness, cm
$\delta_w$	skin thickness, cm
$\varepsilon$	emissivity of test surface

$\eta$	turbulent recovery factor, 0.88
$\theta$	boundary-layer momentum thickness, cm
$\mu$	dynamic viscosity, $1.462 \times 10^{-6} \frac{\sqrt{T}}{1 + 112/T}$ (ref. 12), N-sec/m <sup>2</sup>
$\nu$	kinematic viscosity, m <sup>2</sup> /sec
$\rho$	density of air, kg/m <sup>3</sup>
$\sigma$	Stefan-Boltzman constant, $5.67 \times 10^{-8}$ W/(m <sup>2</sup> - K <sup>4</sup> )
$\tau$	shear stress, N/m <sup>2</sup>

#### Subscripts:

$R$	boundary-layer recovery
$t$	total
$w$	wall or skin
$\delta$	boundary-layer edge
$\infty$	free stream

A bar over a quantity denotes either an incompressible variable or a compressible variable that has been transformed to an equivalent incompressible value.

### DESCRIPTION OF EQUIPMENT

A hollow cylinder 3.04 meters in length and 0.437 meter in outside diameter was installed on the lower fuselage of the YF-12A airplane (fig. 1). The cylinder was attached to a pylon that was mounted to hard points on the aircraft. The pylon provided a vertical separation distance between the aircraft fuselage and the hollow cylinder of 0.46 meter. A photograph of the airplane with the cylinder installed is shown in figure 2. A complete description of the airplane can be found in reference 7.

The cylinder was constructed from 321 stainless steel and had a sharp leading edge with a radius of 0.0127 centimeter. As shown in figure 3, the cylinder consisted of an inner structural tube and an outer nonstructural thin skin shell. The outside diameter of the inner tube was 40.64 centimeters, and the wall thickness was 0.64 centimeter. Three structural ring frames were located at the aft end of the tube. These structural ring frames were attached to the pylon structural box with provisions for the on-the-ground adjustment of the angle of attack of the cylinder. The

outside diameter of the outer shell was 43.7 centimeters, and the thickness of the shell was 0.127 centimeter. Fiber glass isolator spacers were attached to the inside wall of the outer thin skin shell to provide the necessary clearance between the inner tube and the outer shell and to insulate the outer test surface from the inner structure.

The outer shell was constructed in three sections. The lower half of the shell was one continuous piece, whereas the upper half of the shell was divided into two sections so that the aft section could be more easily removed to repair and install instrumentation lines. The leading edge portion of the cylinder was constructed as a separate cylindrical section with a length of 10.16 centimeters, and it could be detached from the main body of the cylinder for refurbishment if necessary. Because of the limited space between the inner tube and the outer shell, it was necessary to construct a 4.2- by 7.4-centimeter channel along the inside of the inner tube (fig. 3) to facilitate the routing of instrumentation lines.

## INSTRUMENTATION

The cylinder was instrumented with thermocouples, static pressure orifices, a skin friction gage, a pitot pressure rake, and a total temperature boundary-layer rake (fig. 4(a)). Most of the boundary-layer measurements were made on the lower centerline of the cylinder, where the boundary-layer rakes and skin friction gage were installed. The static pressure and temperature measurements made at the other locations were used primarily to detect abnormalities in the flow field on the cylinder and to determine cylinder alignment. Data from the thermocouples, pressure orifices, rakes, and skin friction gage were recorded on tape by a pulse code modulation (PCM) data acquisition system. The accuracy of the PCM system was  $\pm 0.3$  percent of full scale. The individual instruments are discussed in the following sections.

### Skin Friction Gage

The skin friction gage used in this experiment was a commercially developed liquid-cooled force balance. The floating element (fig. 4(b)) was kept centered by electromagnets, and any force acting to displace the floating element along its sensitive axis was countered by an increase in voltage to the electromagnets. The voltage necessary to keep the element centered was recorded and converted to shear force by an appropriate calibration. The floating element did not protrude above and was less than 0.00127 centimeter below the surface of the gage body at room temperature. The space between the floating element and the gage body was uniform and less than 0.00254 centimeter. Additional details about the skin friction gage are given in reference 8. As shown in figure 4(b), thermocouples were installed on the gage body, on the cooling jacket, and on the cylinder skin directly beneath the edge of the exposed surface of the gage. The thermocouples were used to monitor the temperature of the skin friction gage.

## Thermocouples

One hundred and twenty-three 22-gage Chromel-Alumel thermocouples were spot welded to the inner surface of the outer skin at the locations shown in figure 4(a). Sixty-seven thermocouples were installed on the lower centerline, and the outputs from these thermocouples were used to derive the heat transfer coefficients and other boundary-layer parameters presented in this report. The accuracy of the temperature measurements was  $\pm 2$  K.

## Static Pressure Orifices

Eight static pressure orifices were installed on the lower centerline of the cylinder, and 26 orifices were installed circumferentially at the locations shown in figure 4(a). The pressure orifices were 0.24 centimeter inside diameter machined fittings installed flush with the outside surface of the skin. Tubes with an outside diameter of 0.24 centimeter were connected to the pressure orifice fittings and then routed to the instrument bay, where they were connected to two 48-port scanivalves with integral  $\pm 6.9 \text{ kN/m}^2$  differential pressure transducers.

Each static pressure orifice was connected to at least two successive ports of the scanivalves, and several of the orifices were also connected to continuously recorded differential verification transducers. A reference pressure orifice located on the lower forward fuselage was connected to the reference side of the differential transducers and to a high resolution absolute pressure transducer with an accuracy of  $12.1 \text{ N/m}^2$ . The reference pressure orifice was also connected to several of the scanivalve ports to provide in-flight zeros for the scanivalve transducers. The overall accuracy of the static pressure measuring system was estimated to be  $\pm 69 \text{ N/m}^2$ .

## Pitot Pressure Rake

A boundary-layer pitot pressure rake was installed on the cylinder's lower centerline 2.74 meters aft of its leading edge (fig. 4(a)). Details of the rake and its dimensions are shown in figure 5(a). The 16 impact pressure tubes (or probes) were 0.1 centimeter in diameter and extended 1.0 centimeter forward of the sharp leading edge of the rake body. The tubes were connected to three 48-port scanivalves with integral differential pressure transducers. The transducers had ranges of 0 to  $20.7 \text{ kN/m}^2$ , 0 to  $41.4 \text{ kN/m}^2$ , and 0 to  $68.9 \text{ kN/m}^2$ . Impact pressure tubes 1 to 7 were connected to the scanivalve with the low range transducer. Tubes 3 to 12 were connected to the scanivalve with the midrange transducer, and tubes 8 to 16 were connected to the scanivalve with the highest range transducer. Each pitot pressure tube was connected to at least two successive ports on the scanivalve. Reference pressure and the in-flight zero measurements were obtained in the same way as was used for the static pressure orifices. The accuracy of the impact pressure measurements was 1 percent of full scale.



As shown in figure 5(a), a conical probe was installed at the end of the rake. The conical probe was used to measure flow angles to establish cylinder alinement; therefore, the rake was installed so that the conical probe was alined with and parallel to the lower centerline of the cylinder ( $\pm 0.1^\circ$ ). Details of the conical probe flow direction sensor are shown in figure 5(b). The flush orifices at  $0^\circ$  and  $180^\circ$  were connected to a single  $\pm 6.9 \text{ kN/m}^2$  differential pressure transducer, and the output from this transducer ( $\Delta p_\alpha$ ) was used to determine the angle of attack. The flush orifices at  $90^\circ$  and  $270^\circ$  were also connected to a  $\pm 6.9 \text{ kN/m}^2$  differential transducer, and the differential pressures measured by this transducer ( $\Delta p_\beta$ ) were used to compute the angle of sideslip. The accuracy of these measurements was estimated to be  $\pm 41 \text{ N/m}^2$ , which corresponds to an angle of  $\pm 0.027^\circ$ . A photograph of the pitot-pressure rake is shown in figure 6.

### Total Temperature Rake

In an attempt to determine the temperature gradient through the boundary layer, a total temperature rake consisting of 17 total temperature probes was installed adjacent to the pitot pressure rake (figs. 4(a), 6, and 7). The probes were installed at intervals of 0.41 centimeter up to a distance from the cylinder of 5.28 centimeters and at intervals of 1.27 centimeters at distances from 5.35 centimeters to 10.36 centimeters.

## DATA REDUCTION

### Boundary-Layer Profiles

Mach numbers through the boundary layer were derived by using the Rayleigh pitot-tube formula (ref. 9) and pressure measurements from the boundary-layer rake and surface static pressure orifices. The usual assumption, that static pressure was constant through the boundary layer, was made.

The velocities through the boundary layer were calculated from the boundary-layer Mach numbers by using the following equation:

$$U = M \sqrt{\gamma R} \left( \frac{T_t}{1 + \frac{\gamma - 1}{2} M^2} \right)^{1/2} \quad (1)$$

In order to solve equation (1), the distribution of total temperature through the boundary layer must be determined. In this investigation, boundary-layer total temperatures were measured. However, because of the thinness of the boundary layer and the comparatively large size of the total temperature probes, a detailed total temperature profile could not be obtained. Therefore, it was necessary to use

a theoretical total temperature distribution. It will be shown in the RESULTS AND DISCUSSION section that the measured temperatures were in good agreement with a quadratic form of the boundary-layer total temperature ratio distribution. Consequently, the total temperatures used to solve equation (1) were computed with the quadratic relationship as given in reference 3. In the notation of this report, this quadratic relationship may be written as follows:

$$\frac{T_t}{T_{t,\delta}} = a \left( \frac{U}{U_\delta} \right)^2 + b \left( \frac{U}{U_\delta} \right) + c \quad (2)$$

where

$$T_{t,\delta} = T_{t,\infty} = T_\infty \left( 1 + \frac{\gamma-1}{2} M_\infty^2 \right)$$

$$a = 1 - \frac{T_R}{T_{t,\delta}}$$

$$b = \frac{T_R}{T_{t,\delta}} - \frac{T_w}{T_{t,\delta}}$$

$$c = T_w/T_{t,\delta}$$

and

$$T_R = T_\delta \left( 1 + \frac{\gamma-1}{2} \eta M_\delta^2 \right)$$

The momentum-to-thickness ratio,  $\frac{\theta}{\delta}$ , was computed by using the following equation:

$$\frac{\theta}{\delta} = \int_0^1 \frac{\rho U}{\rho_\delta U_\delta} \left( 1 - \frac{U}{U_\delta} \right) d \frac{y}{\delta} \quad (3)$$

In order to obtain the momentum thickness from equation (3), it is necessary to determine the boundary-layer total thickness,  $\delta$ . The total thickness was determined from the measured data by using the method given in reference 10, which will be discussed further in the RESULTS AND DISCUSSION section.

Equation (3) is really the momentum equation for a flat plate and not a cylinder. The momentum equation for a cylinder as obtained from reference 11 is given by the following equation:

$$\frac{\theta}{\delta} = \int_0^1 \frac{\rho U}{\rho_\delta U_\delta} \left( 1 - \frac{U}{U_\delta} \right) \left( 1 + \frac{\delta}{r} \frac{y}{\delta} \right) d \frac{y}{\delta}$$

However, because the radius of the cylinder used in this experiment is so much larger than the boundary-layer thickness, values computed by both equations are essentially the same. Therefore, the simpler flat plate equation (eq. (3)) was used to calculate the momentum thicknesses used in this report.

### Skin Friction and Heat Transfer

The shear force measured by the skin friction gage was reduced to shear stress by using the following equation:

$$\tau = \frac{F}{A} \quad (4)$$

where  $A = 0.694 \text{ cm}^2$ , the area of the floating element of the skin friction gage.

The shear stress was reduced to skin friction coefficients by using the equation

$$C_f = \frac{2\tau}{\rho_\delta U_\delta^2} \quad (5)$$

where  $\rho_\delta$  and  $U_\delta$  are the local density and local velocity, respectively, at the edge of the boundary layer. Density and velocity were computed from static pressure and pitot pressures together with the assumptions that the total enthalpy is constant along the boundary layer and that static pressure is constant through the boundary layer.

Heat transfer coefficients were obtained from the temperature measurements by using the following equation for thin skin heating:

$$h_H = \frac{\rho_w C_{p,w} \delta_w \frac{dT_w}{dt} + \sigma \epsilon K T_w^4}{H_R - H_w} \quad (6)$$

This equation neglects internal radiation and conduction losses. For the test conditions in this experiment, internal radiation losses were negligible. Since the outer skin of the cylinder was insulated from the internal structure, there were no conduction losses except near the skin friction balance. It was necessary to cool the skin friction balance to keep it within design limits, and measured temperatures within 15 centimeters of the balance were significantly affected by conduction losses. Therefore, those temperatures were not used to derive heat transfer coefficients.

Experimental Stanton numbers were computed from the following relationship:

$$St = \frac{h_H}{\rho_\delta U_\delta} \quad (7)$$

The recovery enthalpy was computed as follows:

$$H_R = H_\infty + \frac{U_\infty^2 - U_\delta^2}{2} + \eta \frac{U_\delta^2}{2} \quad (8)$$

where

$$H_\infty = f(T_\infty, p_\infty)$$

and

$$H_w = f(T_w, p_\delta)$$

from reference 12 and  $\eta$  equals 0.88.

The skin heating rate  $\frac{dT_w}{dt}$  was determined for each location on the lower centerline of the cylinder where temperatures were measured by fitting a least-square second-degree curve through 50 data points (10 seconds of data) and taking derivatives of the curve fit. The derivative (heating rate) at the midpoint of each curve was used to determine the measured heat transfer coefficients. Heating rates were also determined graphically by plotting wall temperature versus time, fairing curves through the data, and determining the slopes by means of a first-surface mirror. In general, the values computed by the two methods were in excellent agreement. In the few cases where the two methods differed, the graphically determined values were used.

The density  $\rho_w$  of 321 stainless steel is  $0.8 \times 10^4 \text{ kg/m}^3$ , and its specific heat,  $C_{p,w}$ , is 523.8 J/kg-K at a temperature of 378 K (ref. 13). Although specific heat varies with temperature, the temperature range for which the heat transfer coefficients were reduced was  $378 \text{ K} \pm 17 \text{ K}$ , and the variation in specific heat over a range of 34 K is insignificant. Therefore, only a single value of specific heat was used to reduce the data. The emissivity  $\epsilon$  of the test surface had a nominal value of 0.5 (ref. 14), and the skin thickness was 0.127 centimeter.

Heat transfer can be related to skin friction by using the following Reynolds analogy factor:

$$St = s \frac{C_f}{2}$$

or

$$\frac{h_H}{\rho_\delta U_\delta} = s \frac{\tau}{\rho_\delta U_\delta^2}$$

Therefore

$$s = \frac{2St}{C_f} = \frac{h_H U_\delta}{\tau} \quad (9)$$

Equation (9) was used to obtain the experimental Reynolds analogy factor .

### TEST CONDITIONS

To obtain meaningful boundary-layer measurements, the hollow cylinder had to be in a region of uniform flow and had to be alined with the local flow . Flow-field surveys conducted on a 1/25-scale model of the YF-12A airplane in the Langley Unitary Plan Wind Tunnel (ref. 15) and on the YF-12A airplane in flight showed that the local flow field below the airplane was sufficiently uniform at the location where the hollow cylinder was installed. For the tests reported herein, alinement was determined from the circumferential static pressure measurements and the differential pressure measurements obtained from the conical probe flow direction sensor . To aline the cylinder with the local flow , several preliminary flights had to be made . The cylinder was adjusted between the flights until the desired alinement was obtained . A typical static pressure distribution around the cylinder after alinement was achieved is shown in figure 8 . It should be noted that pressures were not obtained at the 140° location for  $x = 0.457$  meter because of instrumentation problems . Angle of attack and angle of sideslip were computed from the measured circumferential pressures using the oblique shock and Prandtl-Meyer expansion theories .

The angle of sideslip calculated from the pressure distribution shown in figure 8 was 0.12°. Angle of attack was calculated to be 0.04° if the data measured at the circumferential angle of 180° (top of cylinder) were omitted . Using the measurements obtained at 180° resulted in an angle of attack of 0.3° at  $x = 0.457$  meter and -0.2° at  $x = 1.678$  meters . It is obvious that the measurements made on the top of the cylinder were affected by some disturbance emanating from the lower fuselage of the airplane . This was not unexpected, and it was for that reason that the conical flow direction sensor was installed . Typical pressure measurements from the conical probe are shown in figure 9 . This figure shows time histories of the differential pressures measured in the angle of attack plane and the differential pressures measured in the angle of sideslip plane . Also shown are the corresponding angles of attack and sideslip . The local angle of attack was less than 0.08°, and the local angle of sideslip was less than 0.06°. Final cylinder alinement was determined by averaging the results obtained from the circumferential static pressures (neglecting

the 180° data) and the results from the conical flow direction sensor. The angle of attack and angle of sideslip determined by this procedure were less than 0.1°.

Two cylinder configurations were used in the experiment. The first, which was tested during flights 1 and 2, is shown in figure 10.<sup>1</sup> With this configuration, the wall or skin temperature is always at or near the radiation equilibrium temperature; consequently, heat transfer data were not obtained during these flights. The second configuration, which was tested during flight 3, is shown in figure 11. In this configuration the cylinder was insulated with a covering to provide low initial wall temperatures. Before takeoff, to insure that in-flight measurements were obtained at cold surface temperatures, the cylinder was cooled to a temperature of 211 K using gaseous nitrogen. When the airplane reached the desired test conditions, the insulation was removed explosively (within 50 msec) before the test data were obtained.

Time histories of free stream Mach number, altitude, and angle of attack for flights 1, 2, and 3 are shown in figures 12(a) to 12(c). Also in each figure is a typical skin temperature time history measured at one of the thermocouples on the lower centerline. The shaded portion of these flight profiles indicates the period during which the data for this experiment were obtained. Figure 12(c) also shows the time at which the insulation was removed. The figure shows how rapidly skin temperature increased after the insulation was removed. It was during this period of rapid heating that the heat transfer and other data were obtained. The free stream conditions at which the data presented in this paper were obtained are given in table 1. The local (cylinder) test conditions at which the data were obtained are given in table 2, and all comparisons between measured and calculated data were based on these local test conditions.

It should be noted that the table 2 values of boundary-layer edge static pressure,  $p_\delta$ , were actually measured on the surface of the cylinder. The usual assumption, that the static pressure through the boundary layer was constant, was made. The wall-to-recovery temperature ratios given in table 2 for flights 1 and 2 are based on the wall temperature measured on the lower centerline of the cylinder at the location of the skin friction balance, and they are slightly lower than the wall-to-recovery temperature ratios on the cylinder forward of this location.

## RESULTS AND DISCUSSION

### Surface Static Pressures

The surface static pressures measured on the lower centerline of the cylinder are shown in figure 13 for flights 1, 2, and 3. The lines in the figure are straight line fairings of the data. As is apparent, the pressures were constant and equal to 4723 N/m<sup>2</sup> for flight 1, 4944 N/m<sup>2</sup> for flight 2, and 4413 N/m<sup>2</sup> for flight 3.

---

<sup>1</sup>The original numbers for flights 1, 2, and 3 were 111, 112, and 121.

## Boundary-Layer Profiles

The Mach number and velocity profiles derived from the data measured during flights 1 and 2 are tabulated in tables 3(a) and 3(b). Also given in table 3 are the boundary-layer temperature distribution derived from equation (2), the momentum thickness, and the pertinent boundary-layer edge conditions. Because of instrumentation problems, boundary-layer profiles were not obtained during flight 3.

Ratios of the total temperatures measured during flights 1 and 2 are plotted in figure 14 as a function of the velocity ratio squared. Also shown, for comparison, is the quadratic profile calculated from equation (2). The figure shows that the ratios of the measurements are in good agreement with the quadratic distribution.

The boundary-layer velocity profiles calculated from the measurements obtained during flights 1 and 2 are presented in figure 15. Also shown is the velocity profile predicted by the power law. When a power law exponent of 8 was used, the agreement between the power law velocity profile and the measurements was excellent.

## Boundary-Layer Thickness

One of the problems often encountered in an evaluation of the various turbulent skin friction and heat transfer theories is determining the virtual origin of turbulent flow. Unless turbulent flow originates at or near the leading edge of the test specimen, a virtual origin of turbulent flow must be determined. The determination of the location of the virtual origin is somewhat arbitrary. As pointed out in references 1 and 4, this problem can be eliminated if comparisons between measurements and calculations are based on momentum thickness Reynolds number. Consequently, one of the primary purposes of the boundary-layer surveys in this test series was to determine momentum thickness. The ratio of momentum thickness to total boundary-layer thickness was computed by using equation (3) and the velocity and temperature distributions given in table 3. To permit momentum thickness to be determined accurately, the total thickness of the boundary layer must be known. In the present investigation the total boundary-layer thickness was computed by using the method developed in reference 10 and illustrated in figure 16. According to this method, the profile obtained by plotting  $\left(1 - \frac{U}{U_\delta}\right)^{1/2}$  against  $y^{3/2}$  should be a straight line in the outer portion of the boundary layer, and the point where  $\left(1 - \frac{U}{U_\delta}\right)^{1/2}$  equals zero will occur where  $y^{3/2}$  equals  $\delta^{3/2}$ . As is apparent from figures 16(a) and 16(b), the total boundary-layer thicknesses obtained by this procedure were 3.00 centimeters for flight 1 and 3.05 centimeters for flight 2.

## Law-of-the-Wall Velocity Profiles

The accuracy of the skin friction deduced from velocity profile measurements depends not only on the accuracy of the velocity measurements but also on the

accuracy of the theory used to predict the law-of-the-wall velocity profiles. Therefore, before accurate skin friction can be obtained from velocity profiles, the accuracy of the various theories must be determined.

Comparisons of measured and calculated law-of-the-wall velocity profiles are shown in figures 17(a) to 17(c). The solid curve in these figures represents Coles' incompressible values, which are given in reference 16 and tabulated for convenience in table 4. The flight data in these figures are the compressible boundary-layer velocities measured during flights 1 and 2 and reduced to their incompressible values by the indicated theory.

Figure 17(a) shows the data that have been transformed by the theory of van Driest (ref. 17). Figure 17(b) shows the transformed data using Eckert's reference enthalpy method (ref. 18), and the data transformed by the wall reference temperature method are shown in figure 17(c). The procedure by which these theories were used to transform the compressible data to their incompressible values is given in reference 19. The data obtained from flight 2 were transformed by using the shear stress that was directly measured by the skin friction balance. Shear stress measurements were not available for flight 1 because the skin friction balance did not work properly during this flight. Therefore, in order to complete the transformation of the data from flight 1, a value of shear stress had to be determined. It is shown in following sections of the report that the skin friction values predicted by the theory of van Driest were in excellent agreement with the measured skin friction. Consequently, the values of the skin friction coefficient predicted by this theory were used to complete the transformation of the flight data obtained during flight 1.

Both the theory of van Driest and Eckert's reference enthalpy method yield good correlation between the measured profiles and Coles' incompressible curve in the logarithmic portion of the boundary layer. However, as shown in figure 17(c), the data transformed by the wall reference temperature method are in poor agreement with the incompressible curve.

### Skin Friction

Skin friction data were obtained directly from the skin friction balance measurements during flights 2 and 3 as well as indirectly from the heat transfer measurements made during flight 3. The skin friction data measured in the form of shear force, obtained during flight 2, are shown in figure 18. Also shown for comparison and evaluation are the values predicted by the theory of van Driest (ref. 20), the Spalding and Chi method (ref. 21), and Eckert's reference enthalpy method (ref. 18). The values predicted by these theories were computed by using the momentum thickness Reynolds number derived from the measured data. Values predicted by the theory of van Driest and the method of Spalding and Chi are in excellent agreement with the measured data. However, Eckert's reference enthalpy method underpredicts the measured data by approximately 10 percent.



Origin of turbulence.—All of the calculated skin friction values shown in figure 18 were based on momentum thickness Reynolds number. However, direct measurements of momentum thickness were not available for the flight 3 test conditions, so the virtual origin of turbulent flow had to be determined in order to make possible the correlation and comparison of the skin friction coefficients obtained from flights 2 and 3 and the comparison of the data with theoretically predicted values. The first step in determining virtual origin was to look at the boundary-layer transition data. If the transition data showed that flow was turbulent at or near the leading edge of the test specimen, the virtual origin could be assumed to be the leading edge.

Figures 19(a) and 19(b) show boundary-layer transition data that were obtained on the lower centerline of the cylinder during flights 2 and 3, respectively. The data from flight 2 were measured at temperatures near radiation equilibrium, whereas the data obtained during flight 3 were measured at cold wall temperature conditions. (Transition data were also obtained during flight 1. However, since these data were virtually identical to the data obtained during flight 2 and because skin friction data were not measured during flight 1, and, therefore, there was no need to determine a virtual origin, the transition data for this flight are not shown.)

In figure 19(a) the transition data for flight 2 are shown in the form of measured wall temperature as a function of distance from the leading edge. As shown, the beginning of transition occurs at a distance of 0.76 meter and a Reynolds number of 3.4 million, and the end of transition occurs at approximately 1.22 meters and a Reynolds number of 5.5 million. It is obvious from these data that the leading edge is not the origin of turbulent flow and that a virtual origin must be determined. Fortunately, the momentum thickness Reynolds number is known for flight 2; consequently, equivalent length Reynolds numbers were determined for each theory that yielded the same results as obtained when using the momentum thickness Reynolds number. The distance from the leading edge determined from these equivalent Reynolds numbers was interpreted as being the virtual origin for the particular theory used. The virtual origins obtained by this procedure are shown in figure 19(a). Figure 19(b) shows the transition data obtained during flight 3. The data are in the form of heat transfer coefficients as a function of distance from the leading edge. It is obvious from these data that transition occurs so close to the leading edge that turbulent flow can be assumed to originate at the leading edge.<sup>1</sup> Consequently, for flight 3 the length of turbulent flow,  $L$ , and the distance from the leading edge,  $x$ , are considered to be equal.

Evaluation of compressible transformation theories.—Comparison between the measured skin friction coefficients and the values predicted by Eckert's reference enthalpy method, the Spalding and Chi method, and the theory of van Driest are shown in figures 20(a), 20(b), and 20(c), respectively. The solid lines in

---

<sup>1</sup>The fact that the boundary-layer transition occurred much closer to the leading edge during flight 3 than during flight 2 was not expected, since it is normally assumed that the boundary layer becomes more stable at the lower wall temperatures. A postflight visual inspection of the cylinder showed no signs of structural damage; the reason for the early transition during flight 3 is unknown.

figures 20(a) to 20(c) represent the incompressible skin friction coefficients predicted by the von Kármán-Schoenherr equation (ref. 2), and the symbols represent the turbulent skin friction measurements that were transformed to their incompressible values by the indicated compressible theory. The transformed measurements should agree with the solid line if the theory used to transform the data is correct. The solid square symbols in figure 20 represent the skin friction balance data obtained during flight 2. The open triangles represent skin friction coefficients that were obtained from the heat transfer measurements using an experimentally determined Reynolds analogy factor of 1.11 (see section following). The solid triangles represent the skin friction coefficients obtained from the skin friction balance measurements during flight 3. As can be seen, all three theories do a good job of predicting the variation of skin friction coefficients with Reynolds number. However, the level of skin friction predicted by each transformation theory differs substantially. As figure 20(a) shows, the data transformed by Eckert's reference enthalpy method are approximately 10 percent higher than the von Kármán-Schoenherr curve, and this is considered to be fair agreement. Figure 20(b) shows that the measurements transformed by the Spalding and Chi method are about 7 percent higher than the incompressible values. The agreement shown in this figure is considered to be good. However, as shown in figure 20(c), the measured data transformed by the theory of van Driest are within  $\pm 2$  percent of the von Kármán-Schoenherr incompressible values and the agreement is considered to be excellent.

### Reynolds Analogy Factor

Most turbulent heat transfer methods are based on some form of Reynolds analogy between skin friction and heat transfer. Consequently, once a skin friction equation is selected, a Reynolds analogy factor is needed to calculate heat transfer coefficients. The determination of a Reynolds analogy factor has been the subject of considerable investigation but has still not been resolved (ref. 22). Therefore, heat transfer and skin friction were measured simultaneously during this investigation, and by using the relationship  $s = \frac{2St}{C_f}$ , an experimental Reynolds analogy

factor was determined, eliminating the need to estimate a Reynolds analogy factor when making the heat transfer calculation. The Reynolds analogy factor determined from the measured skin friction and heat transfer was 1.11.

### Heat Transfer

Figure 21 shows a comparison between the measured heat transfer coefficients in the form of Stanton numbers and the theoretical values predicted by the theory of van Driest (ref. 20) using an experimental Reynolds analogy factor of 1.11. The dashed line represents the laminar Stanton numbers predicted by Eckert's reference enthalpy method. The values predicted by the theory of van Driest are represented by two solid lines. The upper line represents the Stanton numbers that were calculated using a wall-to-recovery temperature ratio of 0.66, and the lower line represents values computed using a temperature ratio of 0.71. As shown, the Stanton numbers predicted by the theory of van Driest are in excellent agreement with the measured heat transfer data.

## SUMMARY OF RESULTS

Turbulent skin friction, heat transfer, and boundary-layer velocity profiles were measured in flight on the lower centerline of a hollow cylinder 3.04 meters in length at a nominal local Mach number of 2.9, at wall-to-recovery temperature ratios of 0.66 to 0.91, and at local Reynolds numbers of 1 to 12 million. Skin friction coefficients were obtained directly from measurements made by a skin friction force balance and indirectly from heat transfer measurements using a Reynolds analogy factor derived from the force balance and heat transfer data. The results of this investigation led to the following conclusions:

1. The theory of van Driest predicted skin friction coefficients that were in excellent agreement with the measured data ( $\pm 2$  percent). The Spalding and Chi method predicted skin friction coefficients that were 7 percent lower than the measured coefficients, and the values predicted by Eckert's reference enthalpy method were 10 percent lower than the measured skin friction coefficients.

2. A measured Reynolds analogy factor of 1.11 was derived from the skin friction and heat transfer data.

3. Heat transfer coefficients predicted by the theory of van Driest using the measured Reynolds analogy factor were in excellent agreement with the measured heat transfer coefficients.

4. Measured velocity profiles transformed by the theory of van Driest and Eckert's reference enthalpy method were in good agreement with Coles' incompressible law-of-the-wall velocity profile.

*Dryden Flight Research Center  
National Aeronautics and Space Administration  
Edwards, Calif., November 5, 1979*

## REFERENCES

1. Hopkins, Edward J.; Rubesin, Morris W.; Inouye, Mamoru; Keener, Earl R.; Mateer, George C.; and Polek, Thomas E.: Summary and Correlation of Skin-Friction and Heat Transfer Data for a Hypersonic Turbulent Boundary Layer on Simple Shapes. NASA TN D-5089, 1969.
2. Peterson, John B., Jr.: A Comparison of Experimental and Theoretical Results for the Compressible Turbulent-Boundary-Layer Skin Friction With Zero Pressure Gradient. NASA TN D-1795, 1963.
3. Samuels, Richard D.; Peterson, John B., Jr.; and Adcock, Jerry B.: Experimental Investigation of the Turbulent Boundary Layer at a Mach Number of 6 With Heat Transfer at High Reynolds Numbers. NASA TN D-3858, 1967.
4. Hopkins, Edward J.; Keener, Earl R.; and Louie, Pearl T.: Direct Measurements of Turbulent Skin Friction on a Nonadiabatic Flat Plate at Mach Number 6.5 and Comparisons With Eight Theories. NASA TN D-5675, 1970.
5. Quinn, Robert D.; and Olinger, Frank V. (appendix A by James C. Dunavant and Robert L. Stallings, Jr.): Heat-Transfer Measurements Obtained on the X-15 Airplane Including Correlations With Wind-Tunnel Results. NASA TM X-1705, 1969.
6. Banner, Richard D.; Kuhl, Albert E.; and Quinn, Robert D.: Preliminary Results of Aerodynamic Heating Studies on the X-15 Airplane. NASA TM X-638, 1962.
7. NASA YF-12 Flight Loads Program. NASA TM X-3061, 1974.
8. Garringer, Darwin J.; and Saltzman, Edwin J.: Flight Demonstration of a Skin-Friction Gage to a Local Mach Number of 4.9. NASA TN D-3830, 1967.
9. Ames Research Staff: Equations, Tables, and Charts for Compressible Flow. NACA Rept. 1135, 1953. (Supersedes NACA TN 1428.)
10. Peterson, John B., Jr.: Boundary-Layer Velocity Profiles Downstream of Three-Dimensional Transition Trips on a Flat Plate at Mach 3 and 4. NASA TN D-5523, 1969.
11. Adcock, Jerry B.; Peterson, John B., Jr.; and McRee, Donald I.: Experimental Investigation of a Turbulent Boundary Layer at Mach 6, High Reynolds Numbers, and Zero Heat Transfer. NASA TN D-2907, 1965.
12. Hansen, C. Frederick: Approximations for the Thermodynamic and Transport Properties of High-Temperature Air. NASA TR R-50, 1959. (Supersedes NACA TN 4150).

13. Sachs, G.; and Pray, R. Ford, III, eds.: Air Weapons Materials Application Handbook Metals and Alloys, First ed., TR 59-66, USAF Air Res. and Develop. Command, Dec. 1959. (Available from ASTIA as AD 252301.)
14. Wood, W. D.; Deem, H. W.; and Lucks, C. F.: Thermal Radiative Properties of Selected Materials. DMIC Rept. 177, Vol. 1, Defense Metals Information Center (Columbus, Ohio), Nov. 15, 1962.
15. Lamb, Milton; Stallings, Robert L., Jr.; and Richardson, Celia S.: Aerodynamic Characteristics of 1/25-Scale Model of YF-12 Airplane at Mach 1.80 to 2.96 With and Without External Instrument Packages and Flow-Field Surveys at Mach 2.96. NASA TM X-2524, 1972.
16. Coles, Donald: Measurements in the Boundary Layer on a Smooth Flat Plate in Supersonic Flow. I. The Problem of the Turbulent Boundary Layer. Rept. no. 20-69, Jet Prop. Lab., Calif. Inst. Technol., June 1, 1953.
17. van Driest, E. R.: Turbulent Boundary Layer in Compressible Fluids. J. Aeronaut. Sci., vol. 18, no. 3, Mar. 1951, pp. 145-160, 216.
18. Eckert, Ernest R. G.: Survey of Boundary Layer Heat Transfer at High Velocities and High Temperatures. WADC Tech. Rep. 59-624, Wright Air Dev. Center, U.S. Air Force, Apr. 1960. (Available from ASTIA as AD 238292.)
19. Keener, Earl R.; and Hopkins, Edward J.: Turbulent Boundary-Layer Velocity Profiles on a Nonadiabatic Flat Plate at Mach Number 6.5. NASA TN D-6907, 1972.
20. van Driest, E. R.: The Problem of Aerodynamic Heating. Aeron. Eng. Rev., vol. 15, no. 10, Oct. 1956, pp. 26-41.
21. Spalding, D. B.; and Chi, S. W.: The Drag of a Compressible Turbulent Boundary Layer on a Smooth Flat Plate With and Without Heat Transfer. J. Fluid Mech., vol. 18, part I, Jan. 1964, pp. 117-143.
22. Cary, Aubrey M., Jr.: Summary of Available Information on Reynolds Analogy for Zero-Pressure-Gradient, Compressible, Turbulent-Boundary-Layer Flow. NASA TN D-5560, 1970.

TABLE 1.—FREE STREAM CONDITIONS

Flight	$M_\infty$	$p_\infty$ , N/m <sup>2</sup>	$T_\infty$ , K	$\alpha_{\text{wing}}$ , deg	$\beta$ , deg	$N_{Re_\infty}$ , per m
1	3.00	4020	222	4.0	0	$3.90 \times 10^6$
2	3.02	4178	218	3.9	0	4.19
3	2.98	4092	217	3.8	0	4.07

TABLE 2.—LOCAL CYLINDER CONDITIONS

Flight	$M_\delta$	$T_w/T_R$	$p_\delta$ , N/m <sup>2</sup>	$T_\delta$ , K	$\alpha$ , deg	$\beta$ , deg	$N_{Re_\delta}$ , per m	$N_{Re_\theta}$
1	2.89	0.894	4723	233	0.1	0.1	$4.14 \times 10^6$	7956
2	2.90	0.907	4944	229	0.1	0.1	4.46	8664
3	2.92	0.66 to 0.77	4413	222	0.1	0.1	4.17	(a)

<sup>a</sup>Since boundary-layer velocity profiles were not obtained, the experimental momentum thickness Reynolds number was not available; however, sufficient data were obtained from the pitot pressure rake to determine the boundary-edge Mach number.

TABLE 3.—BOUNDARY-LAYER MACH NUMBER AND VELOCITY DISTRIBUTIONS

(a) Flight 1.  $x = 274$  cm,  $M_\delta = 2.89$ ,  $T_\delta = 233$  K,  $T_w = 514$  K,  
 $T_w/T_R = 0.89$ ,  $p_\delta = 4723$  N/m<sup>2</sup>,  $U_\delta = 884$  m/sec,  $\theta = 0.192$  cm,  $\delta = 3.00$  cm

$y$ , cm	$\frac{y}{\delta}$	$\frac{M}{M_\delta}$	$\frac{T}{T_\delta}$	$\frac{U}{U_\delta}$
0.254	0.084	0.567	1.640	0.726
0.432	0.143	0.619	1.551	0.771
0.610	0.201	0.664	1.475	0.807
0.787	0.260	0.702	1.413	0.834
0.965	0.318	0.737	1.360	0.859
1.321	0.436	0.799	1.265	0.899
1.956	0.646	0.907	1.110	0.955
2.591	0.855	0.983	1.022	0.992
3.226	1.065	1.000	1.000	1.000
3.861	1.274	1.003	0.998	1.002
4.496	1.474	1.007	0.993	1.003

TABLE 3.—Concluded

(b) Flight 2.  $x = 274$  cm,  $M_\delta = 2.90$ ,  $T_\delta = 229$  K,  $T_w = 514$  K,  
 $T_w/T_R = 0.91$ ,  $p_\delta = 4944$  N/m<sup>2</sup>,  $U_\delta = 880$  m/sec,  $\theta = 0.194$  cm,  $\delta = 3.05$  cm

$y$ , cm	$\frac{y}{\delta}$	$\frac{M}{M_\delta}$	$\frac{T}{T_\delta}$	$\frac{U}{U_\delta}$
0.254	0.083	0.566	1.638	0.724
0.432	0.142	0.617	1.551	0.769
0.610	0.200	0.666	1.464	0.805
0.787	0.258	0.700	1.415	0.833
0.965	0.316	0.734	1.359	0.857
1.321	0.433	0.797	1.267	0.896
1.956	0.641	0.903	1.119	0.956
2.591	0.849	0.979	1.024	0.990
3.226	1.058	1.000	1.000	1.000
3.861	1.266	1.003	0.995	1.001
4.496	1.474	1.003	0.995	1.001

TABLE 4.—INCOMPRESSIBLE LAW-OF-THE-WALL VELOCITY PROFILE

[Ref. 16]

$\frac{\bar{U}_\tau y}{\bar{\nu}}$	$\frac{\bar{U}}{\bar{U}_\tau}$	$\frac{\bar{U}_\tau y}{\bar{\nu}}$	$\frac{\bar{U}}{\bar{U}_\tau}$
0	0	50	14.87
1	0.99	60	15.33
2	1.96	80	16.04
3	2.90	100	16.60
4	3.80	150	17.61
5	4.65	200	18.33
6	5.45	300	19.34
7	6.19	400	20.06
8	6.87	500	20.62
9	7.49	600	21.08
10	8.05	800	21.79
12	9.00	1,000	22.35
14	9.76	1,500	23.36
16	10.40	2,000	24.08
18	10.97	3,000	25.09
20	11.49	4,000	25.81
24	12.37	5,000	26.37
28	12.99	6,000	26.83
32	13.48	8,000	27.54
36	13.88	10,000	28.10
40	14.22		

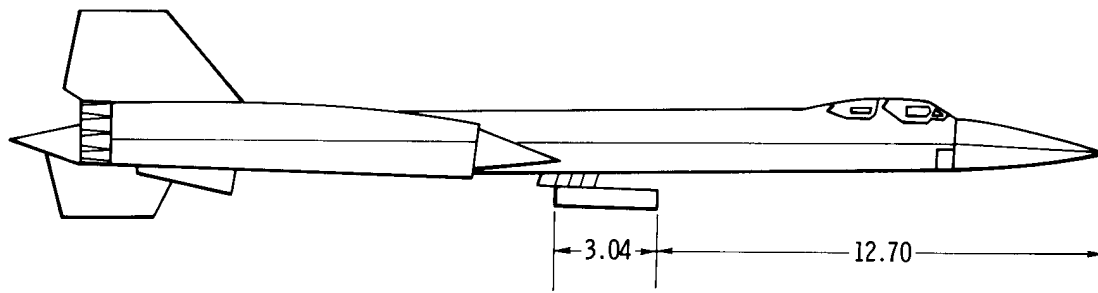


*Figure 1. YF-12A airplane showing location of hollow cylinder.  
Dimensions in meters.*



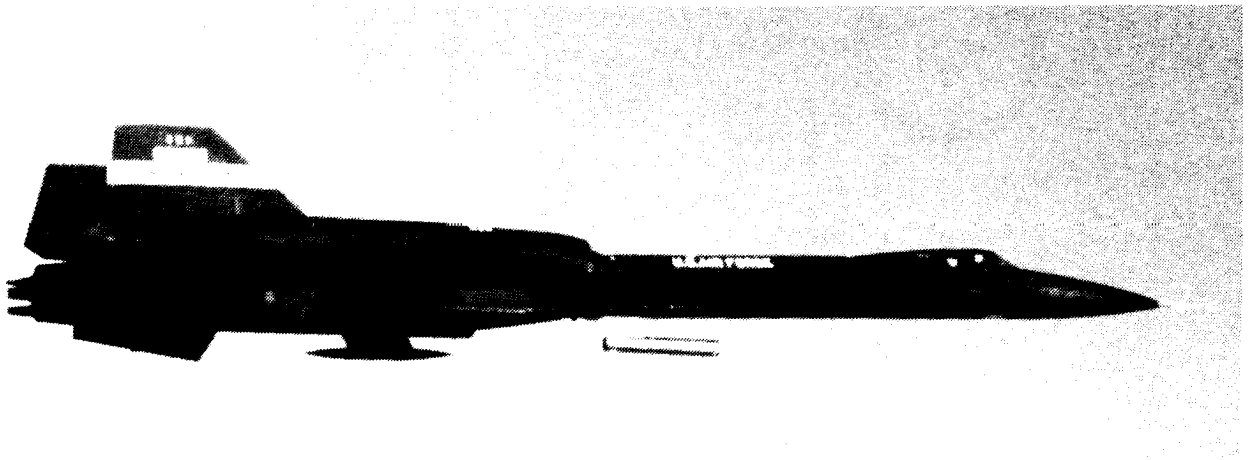


*Figure 2. YF-12A airplane with hollow cylinder attached.*

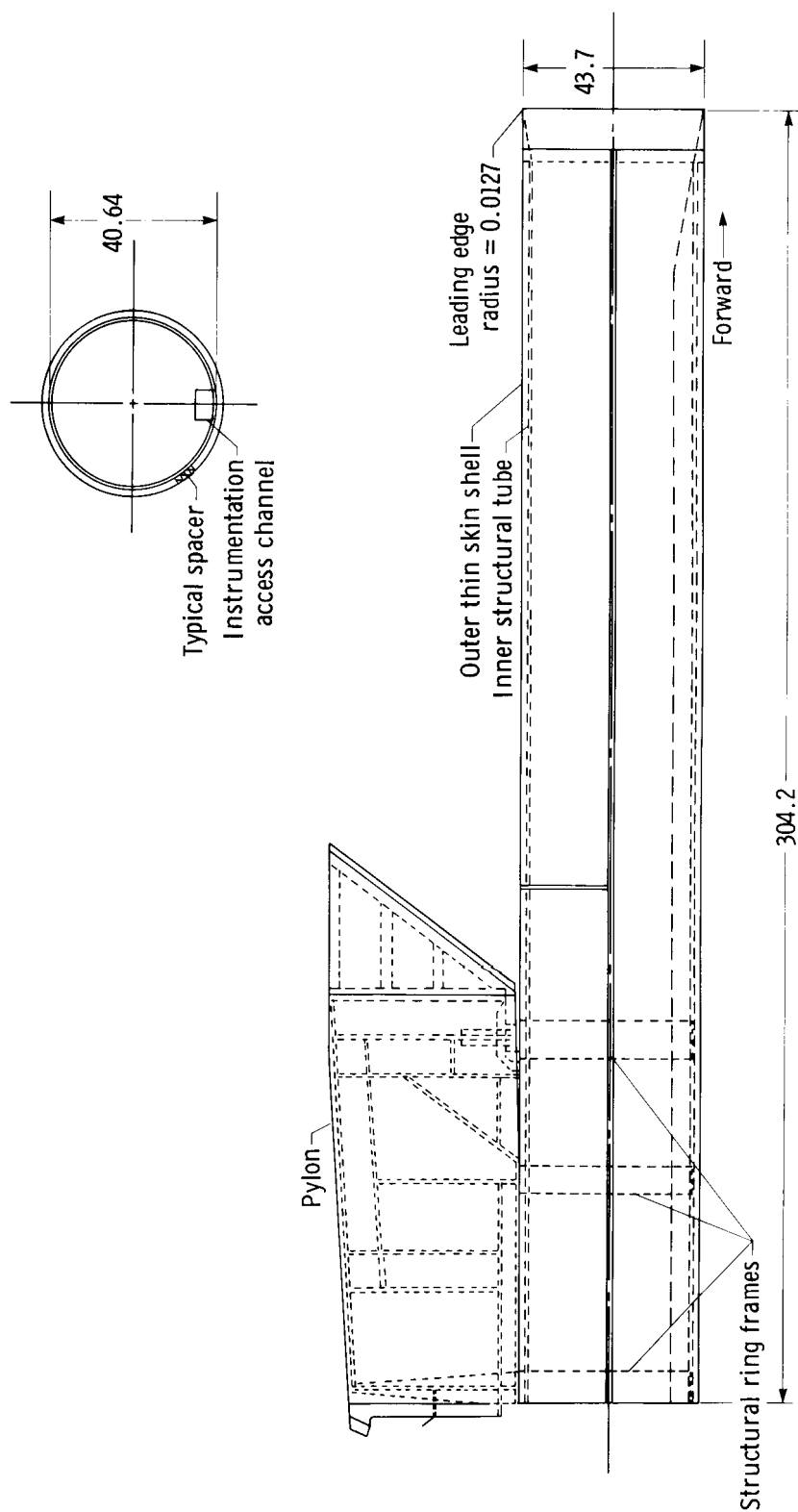


Figure 3. Structural configuration of test specimen. Dimensions in centimeters.

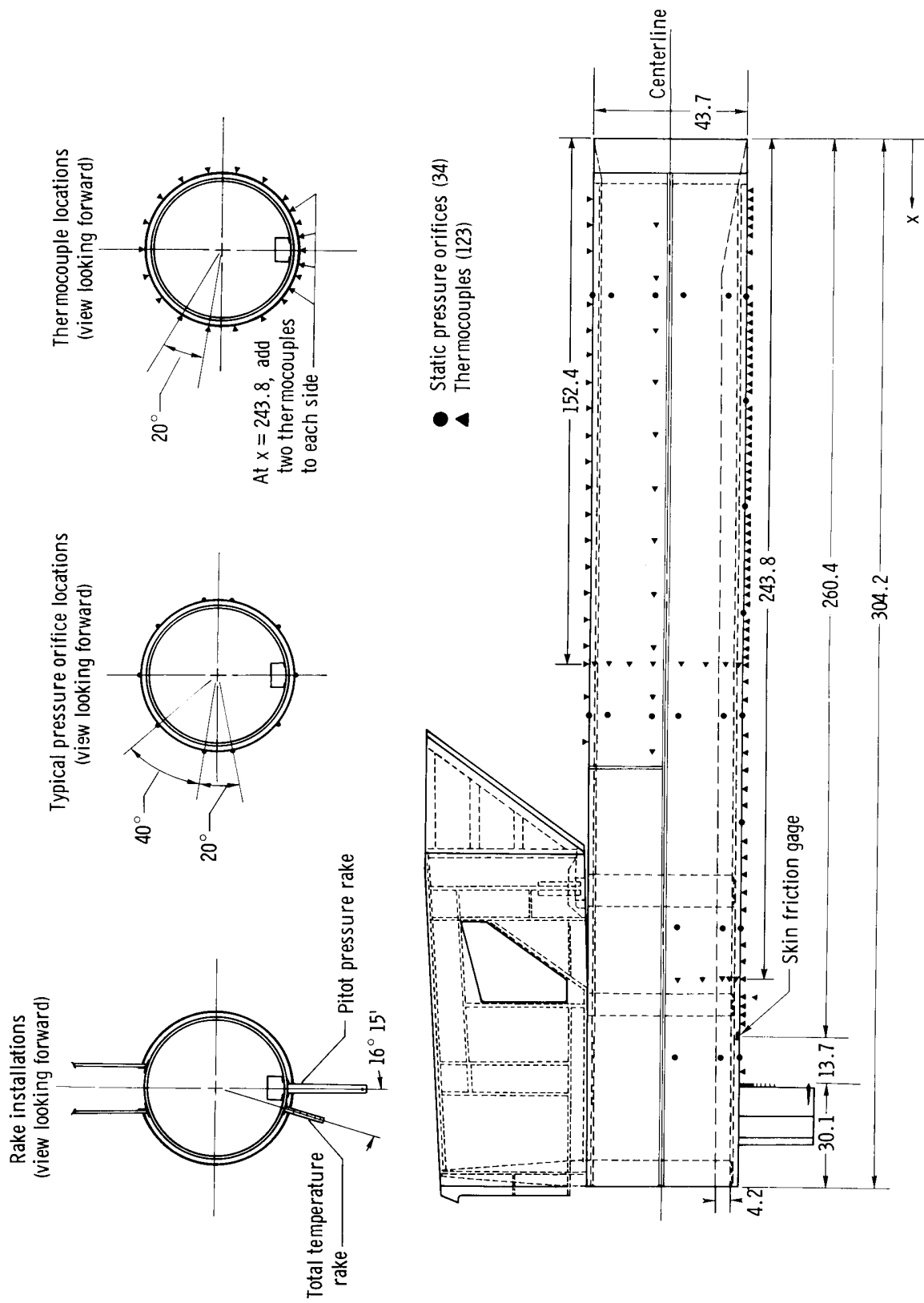
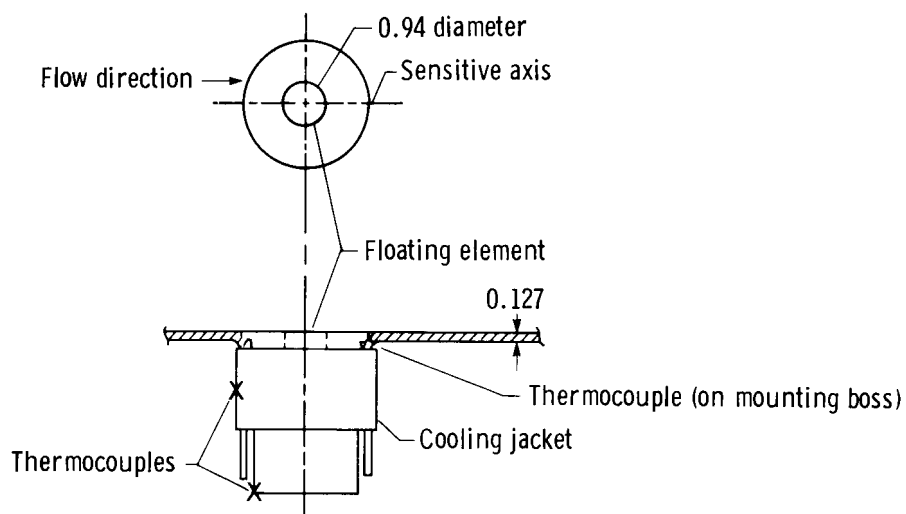


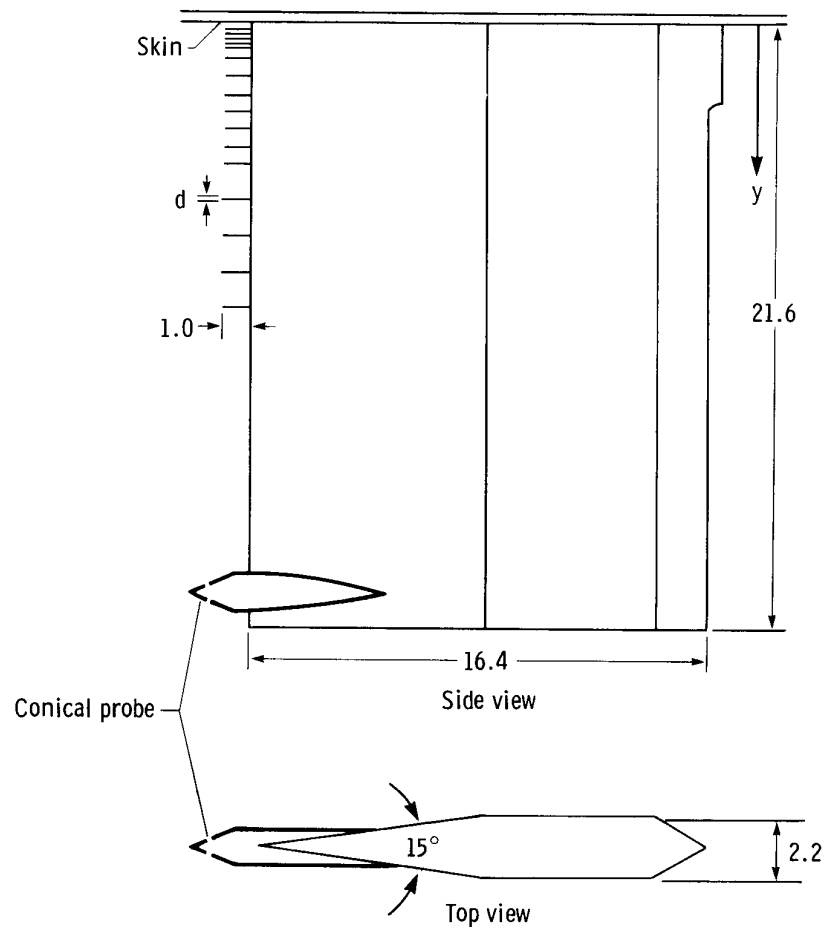
Figure 4. Dimensions and instrumentation of hollow cylinder and skin friction gage. Dimensions in centimeters.



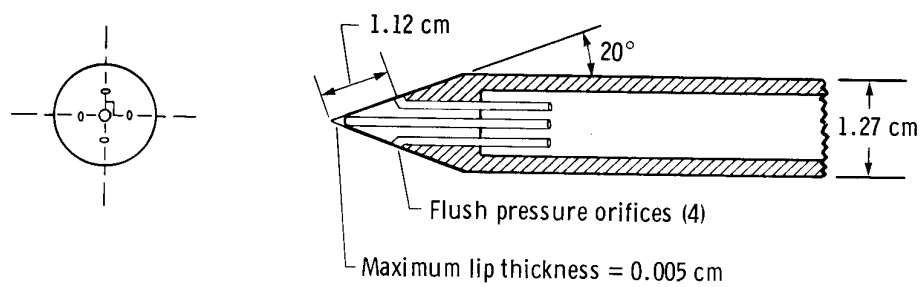
*(b) Skin friction gage.*

*Figure 4. Concluded.*

Probe number	y, cm
1	0.25
2	0.43
3	0.61
4	0.79
5	0.97
6	1.32
7	1.96
8	2.59
9	3.23
10	3.86
11	4.50
12	5.13
13	6.40
14	7.67
15	8.94
16	10.21



(a) Pitot pressure rake.  $d = 0.10$  cm.



(b) Conical probe flow direction sensor. Inside diameter of pressure orifices = 0.13 cm.

Figure 5. Boundary-layer pressure rake. Dimensions in centimeters.

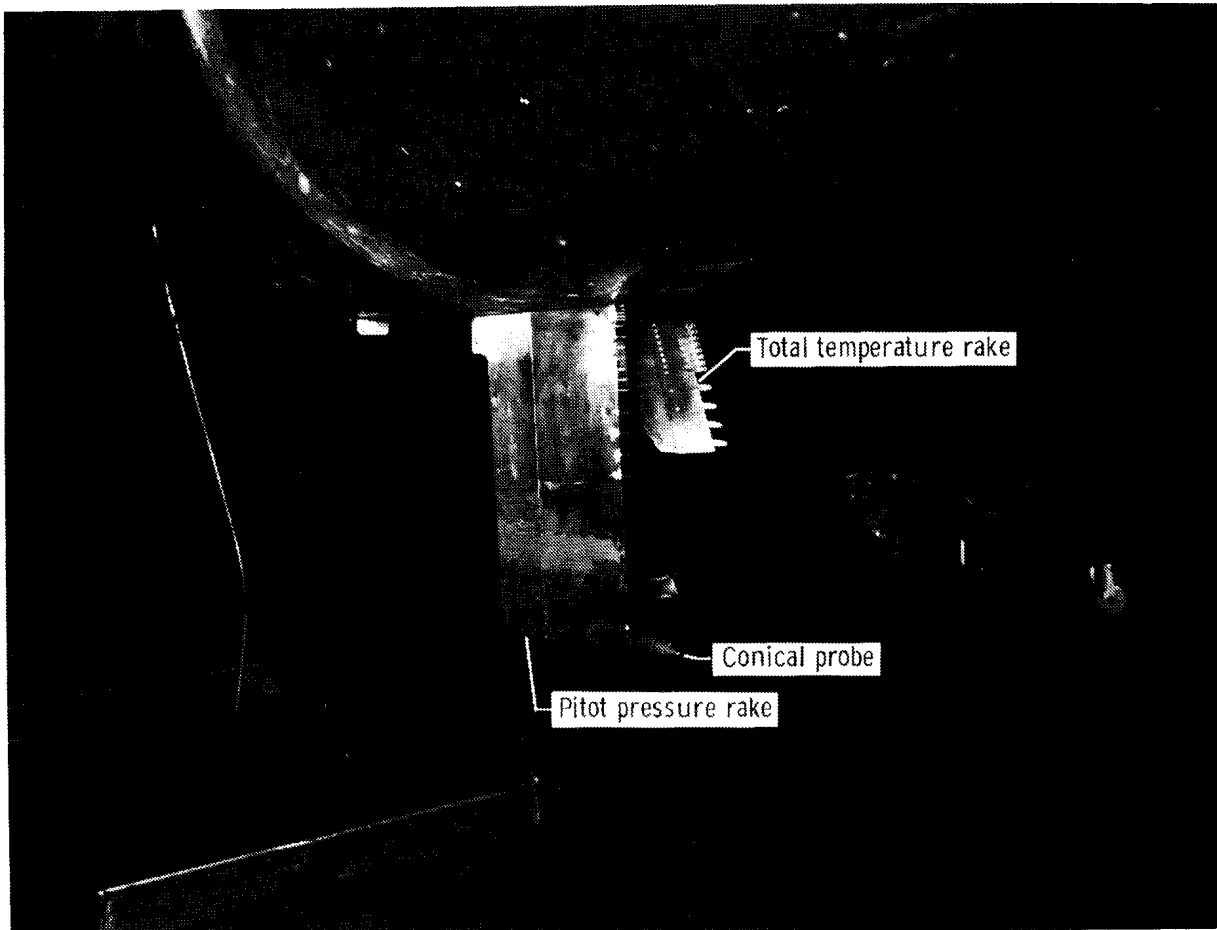


*Figure 6. Pitot pressure and total temperature rakes.*

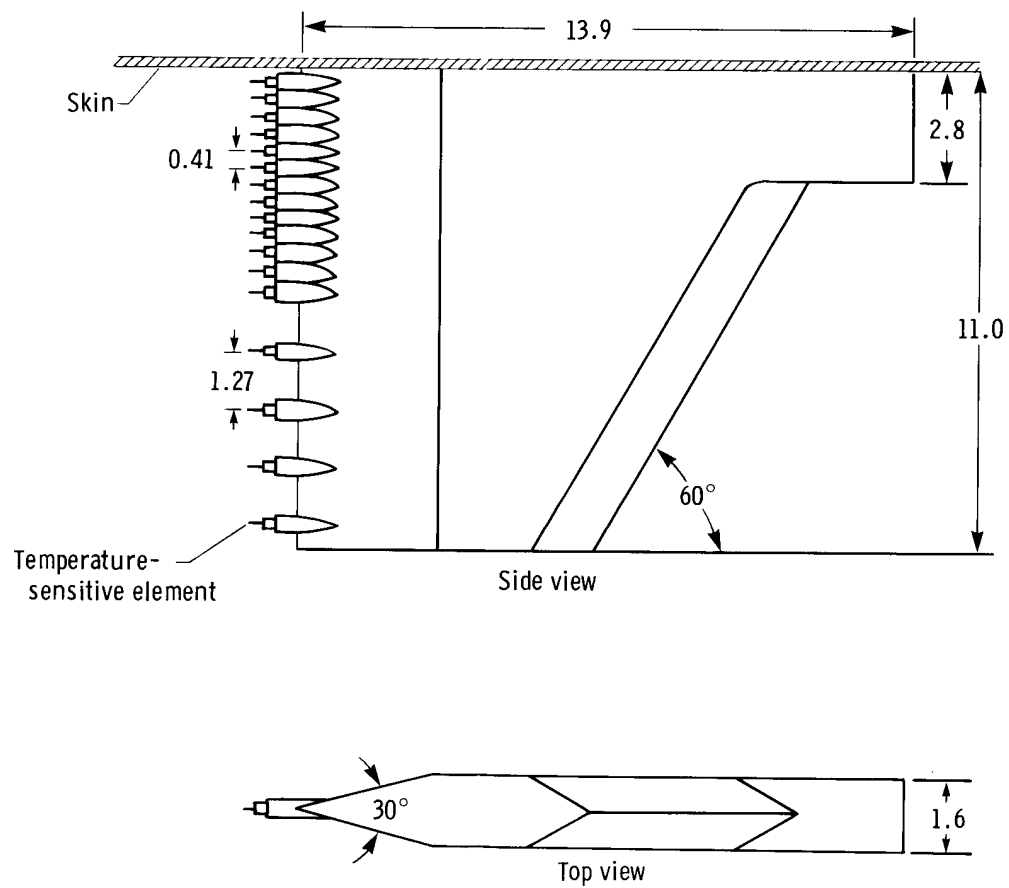


Figure 7. Total temperature rake. Dimensions in centimeters.

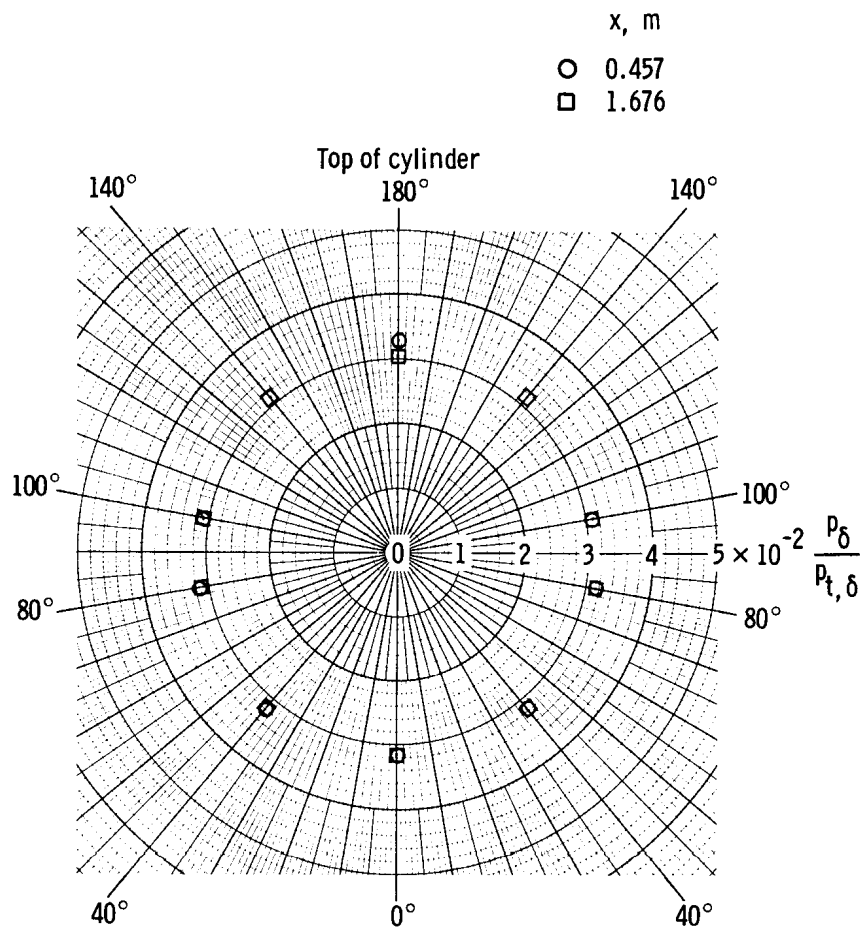


Figure 8. Typical circumferential static pressure distributions (looking forward).



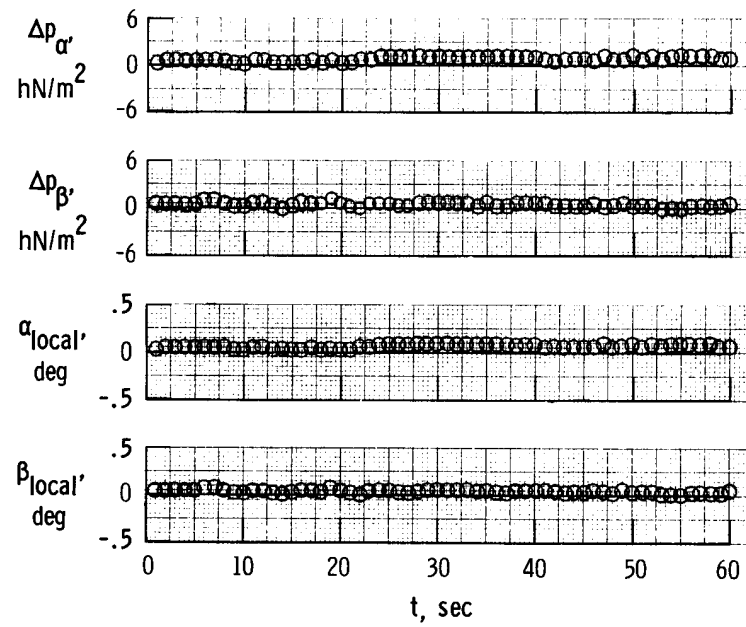
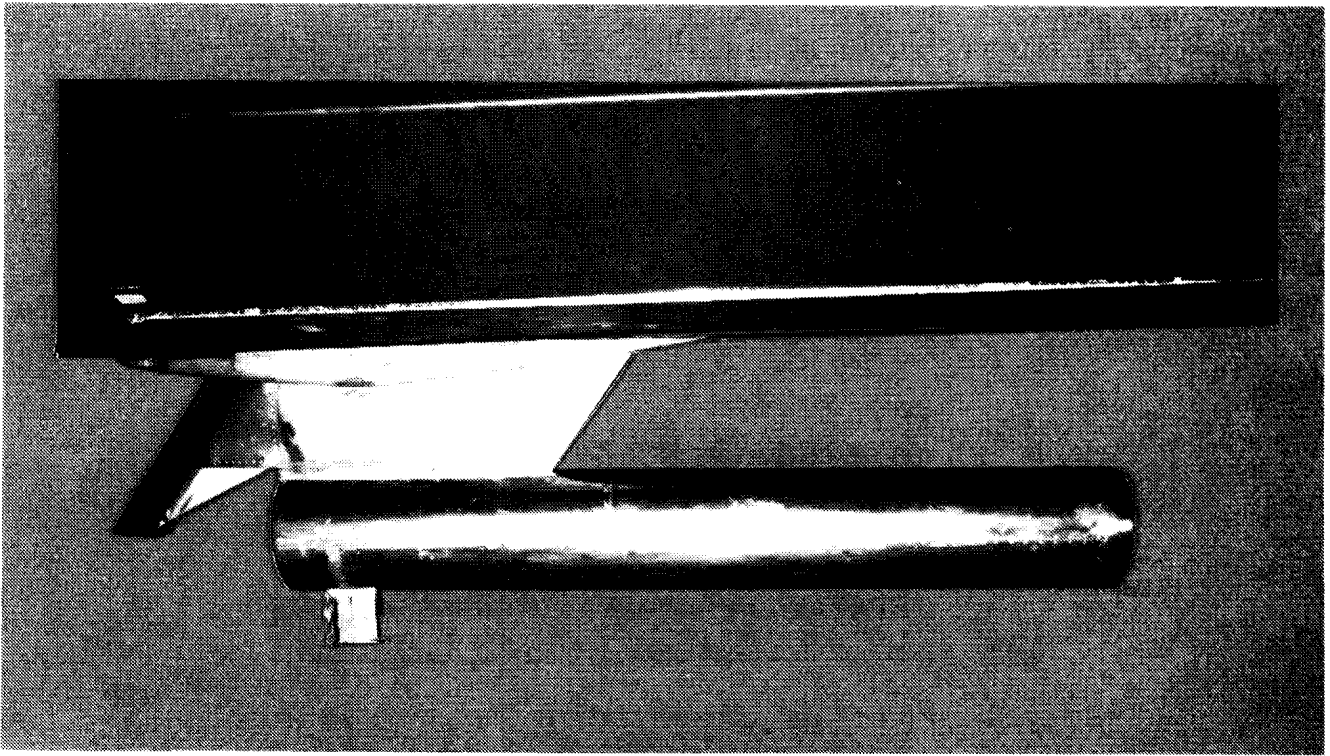
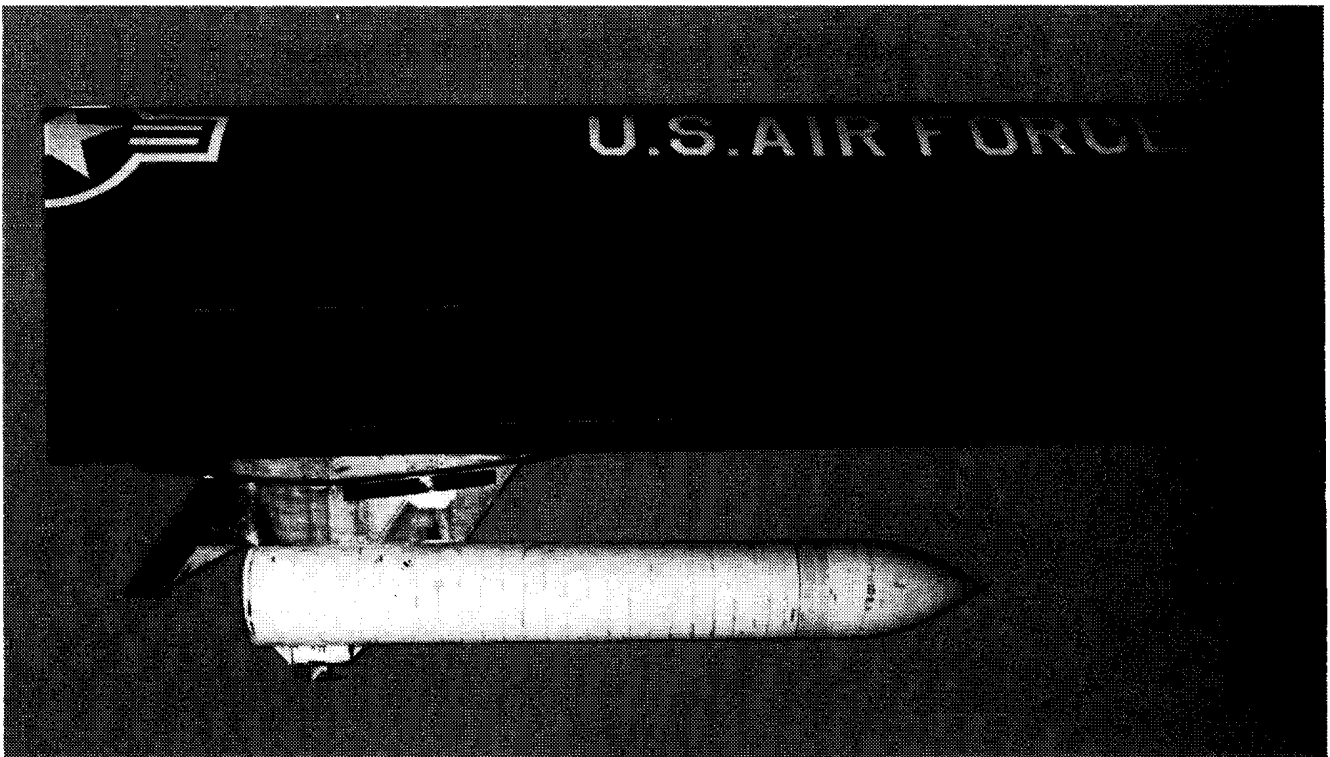


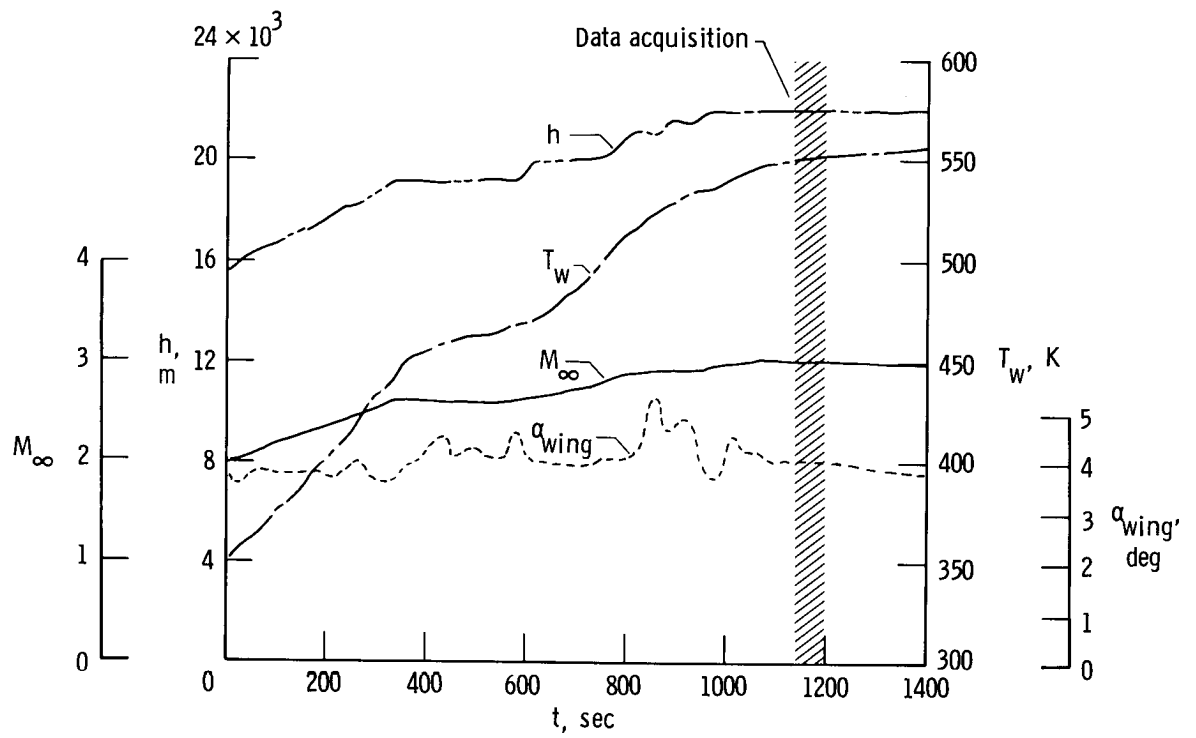
Figure 9. Typical cylinder alinement as determined from conical probe measurements.



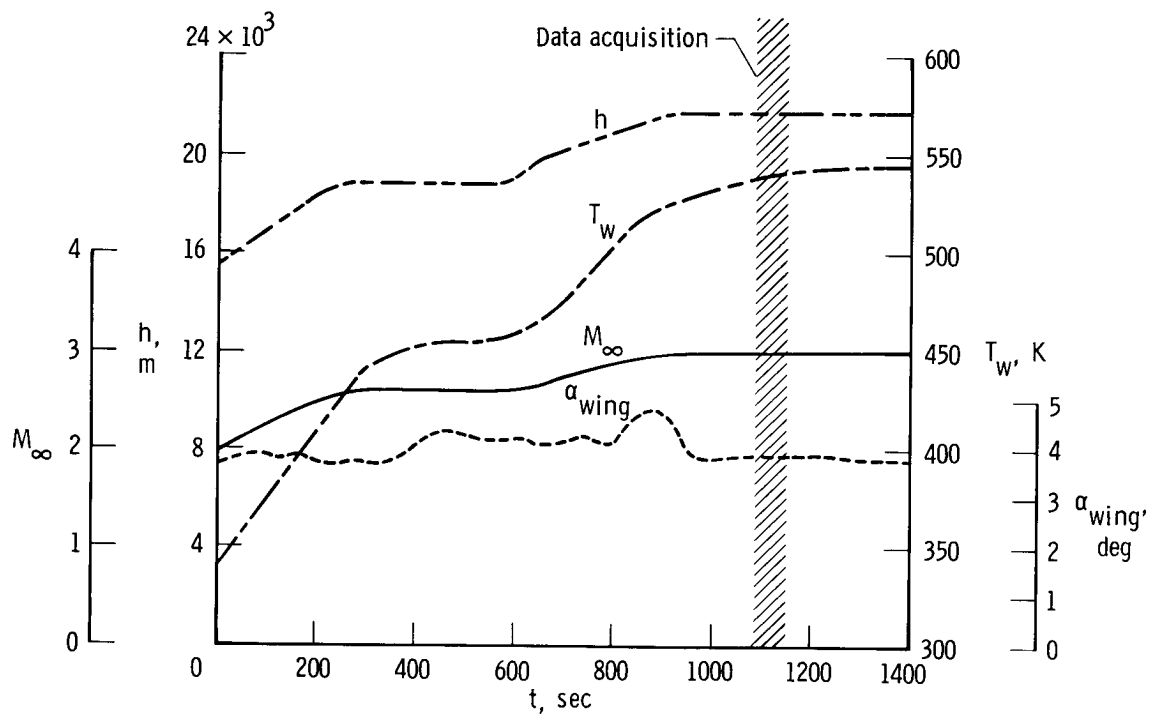
*Figure 10. Cylinder without insulation.*



*Figure 11. Cylinder with insulation.*

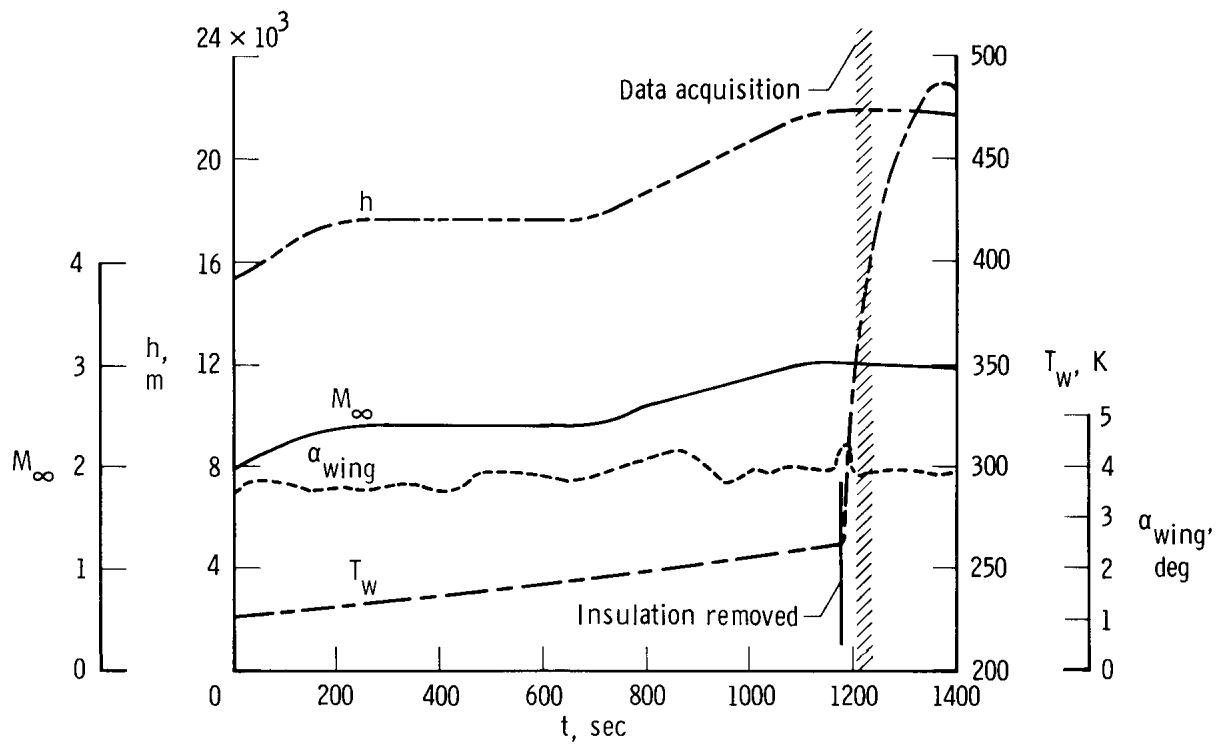


(a) Flight 1.



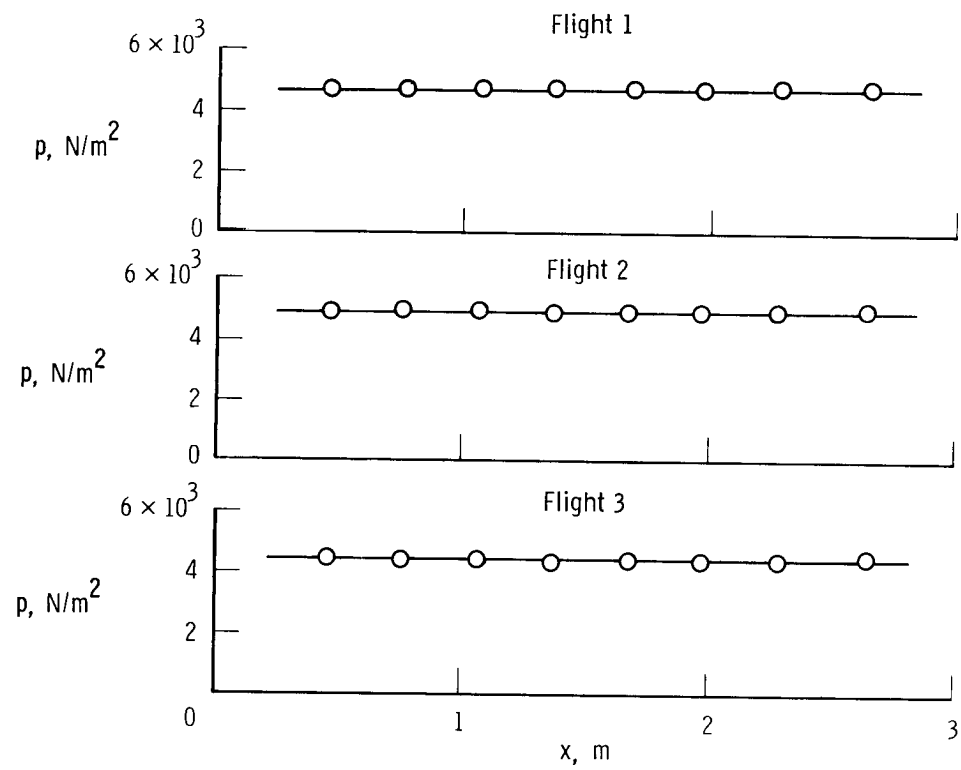
(b) Flight 2.

Figure 12. Time history of flight parameters and typical skin temperatures.



(c) Flight 3.

Figure 12. Concluded.



*Figure 13. Surface static pressures measured on the lower cylinder centerline.*

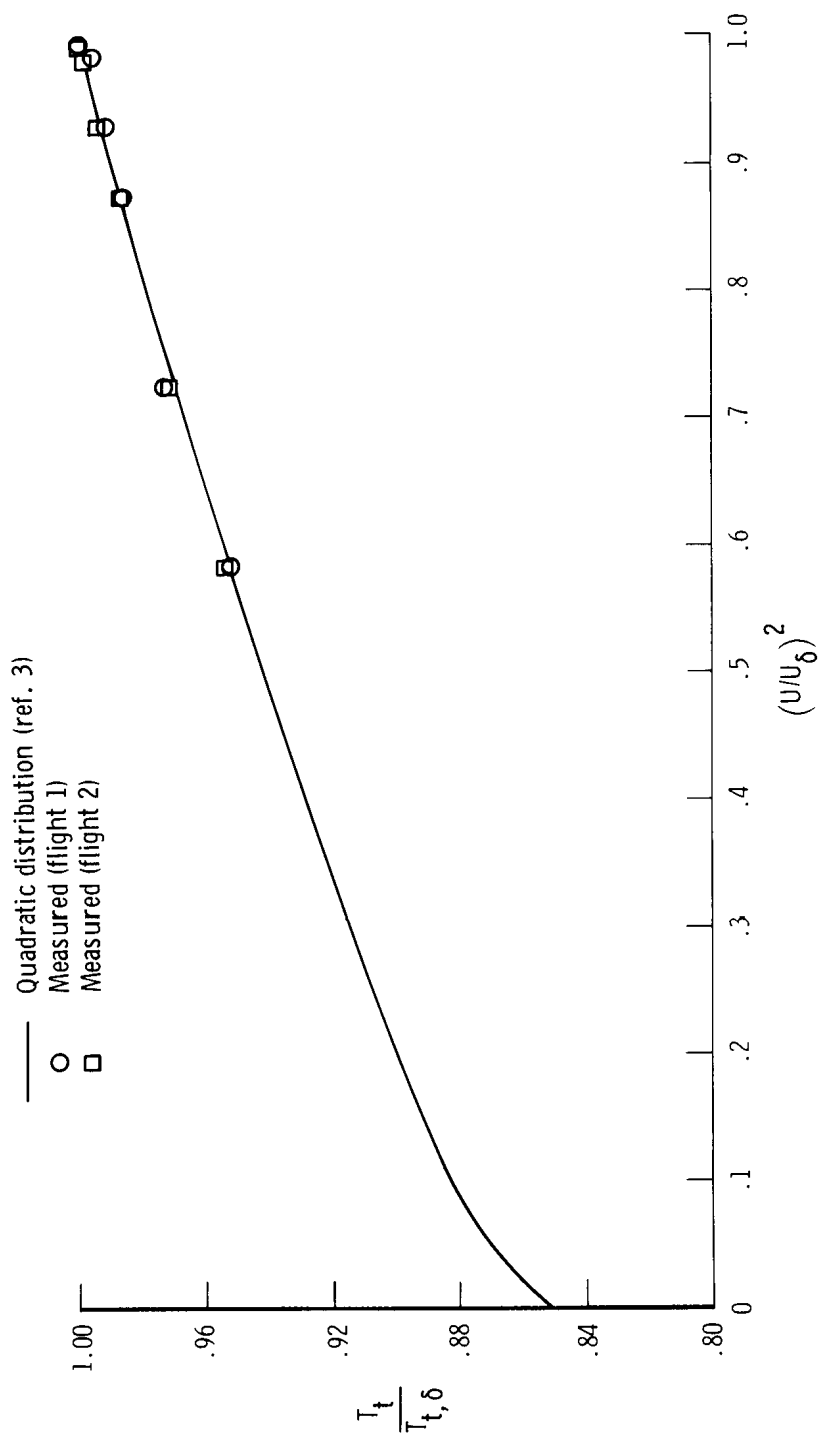


Figure 14. Comparison of theoretical and measured boundary-layer total temperature ratios.

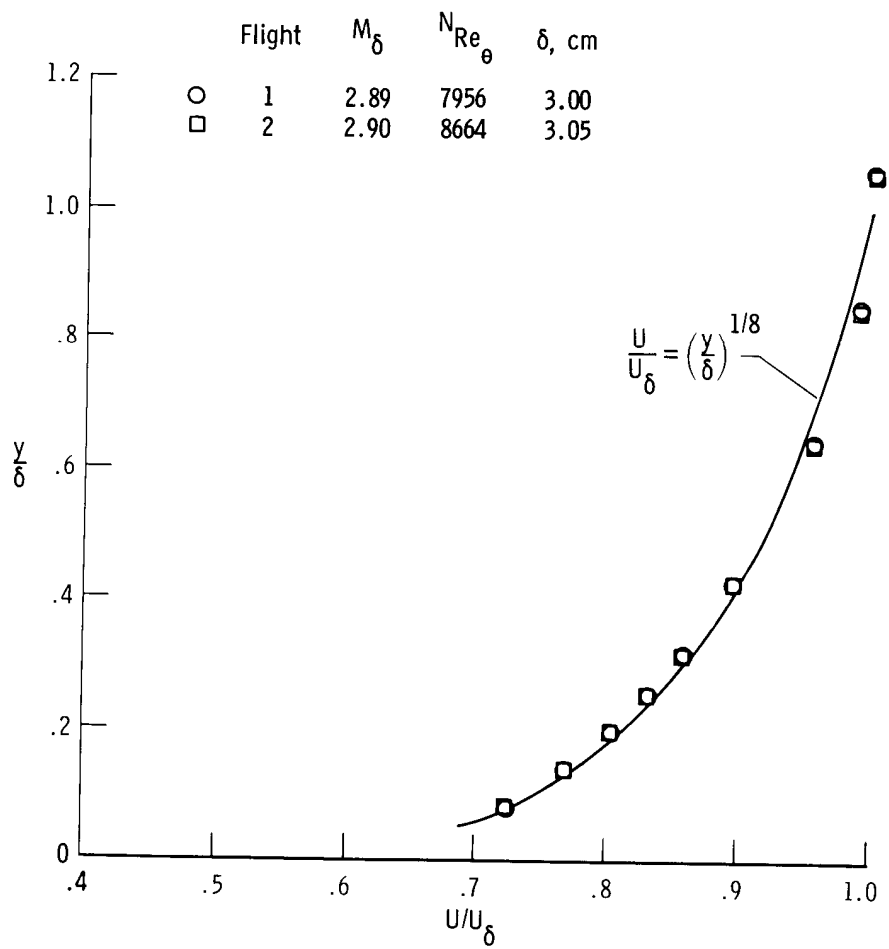
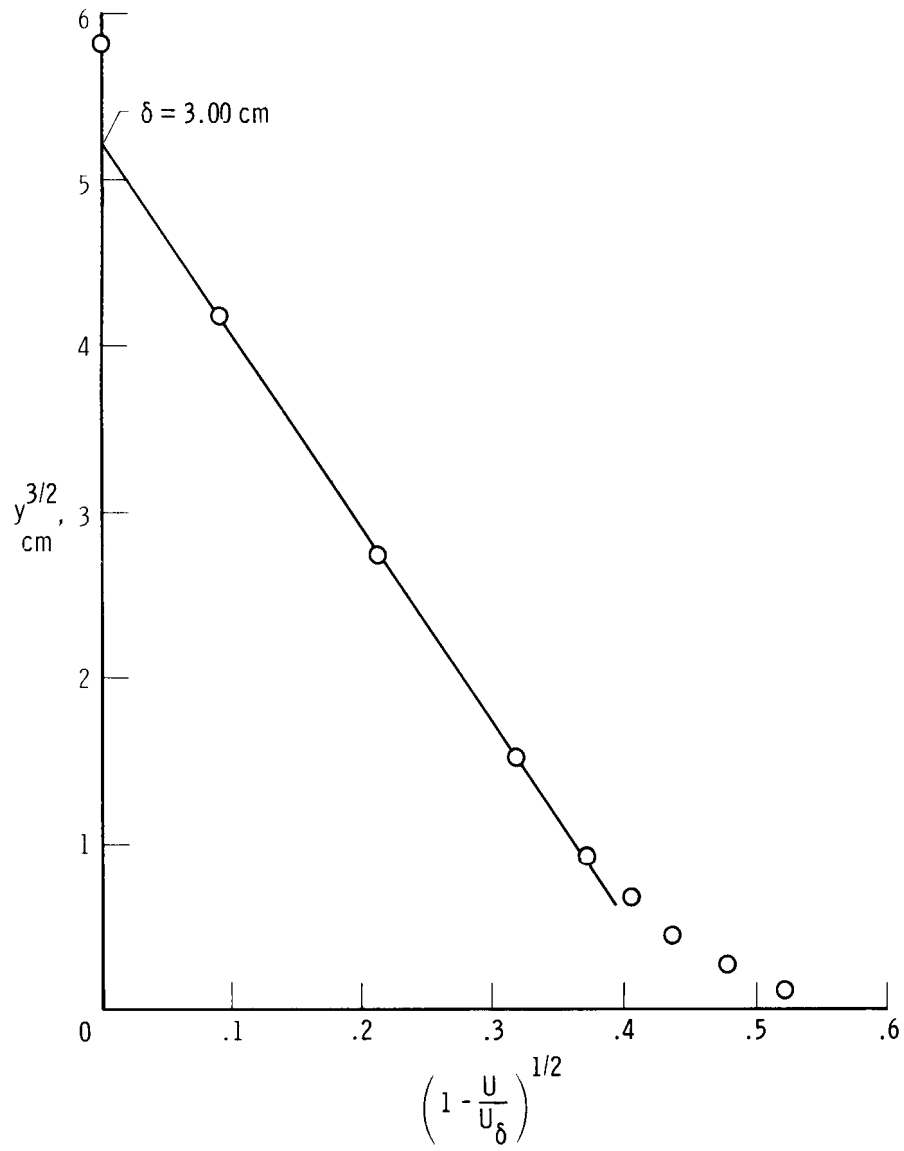


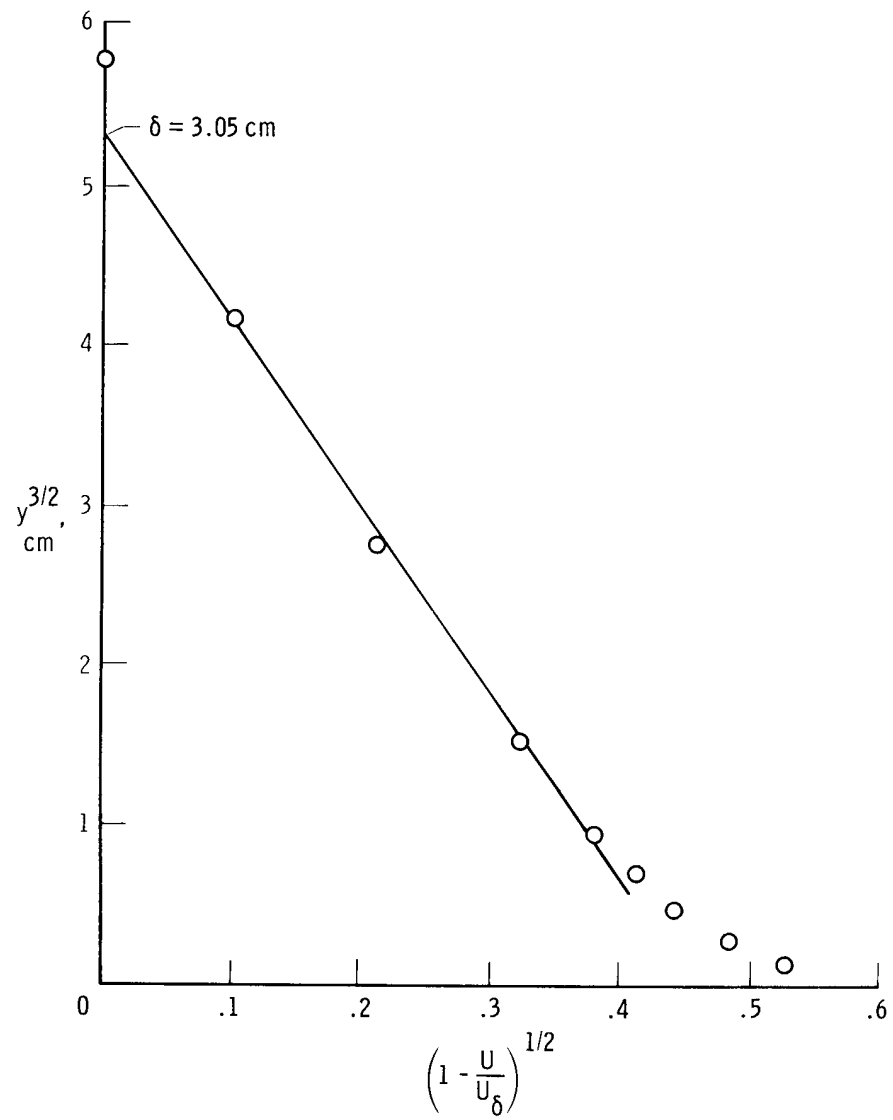
Figure 15. Boundary-layer velocity profiles.



(a) Flight 1.

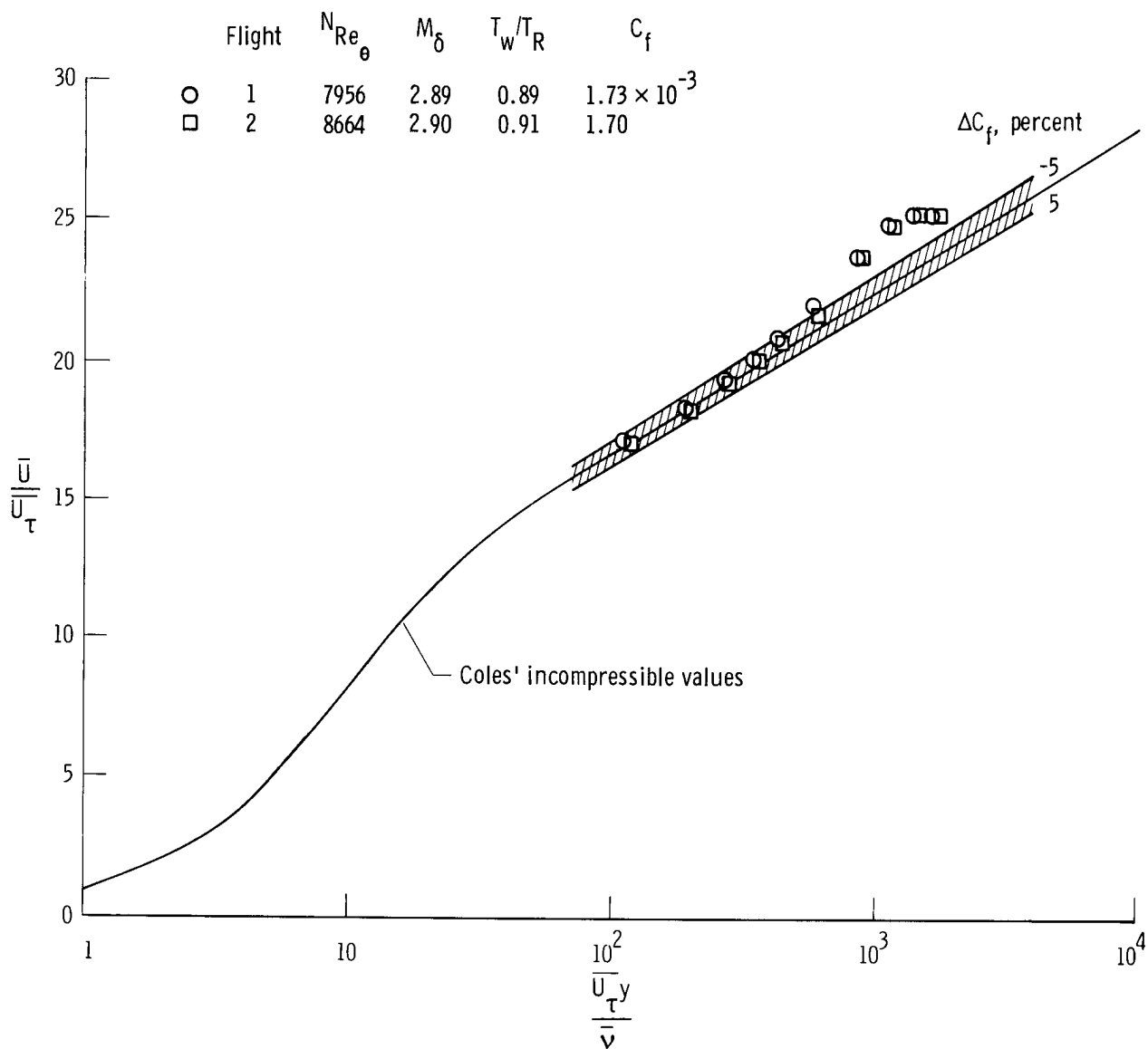
Figure 16. Determination of boundary-layer thickness.





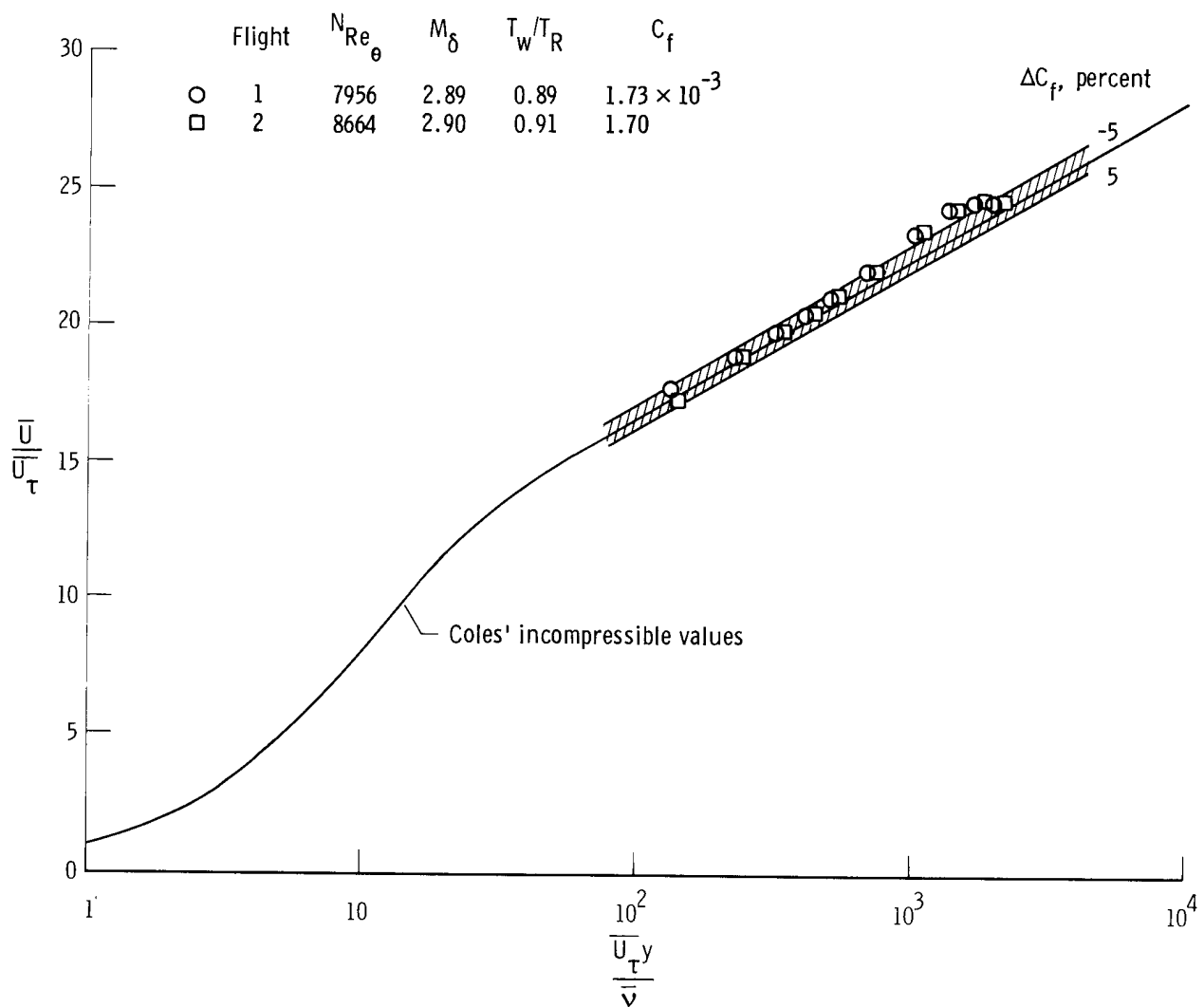
(b) Flight 2.

Figure 16. Concluded.



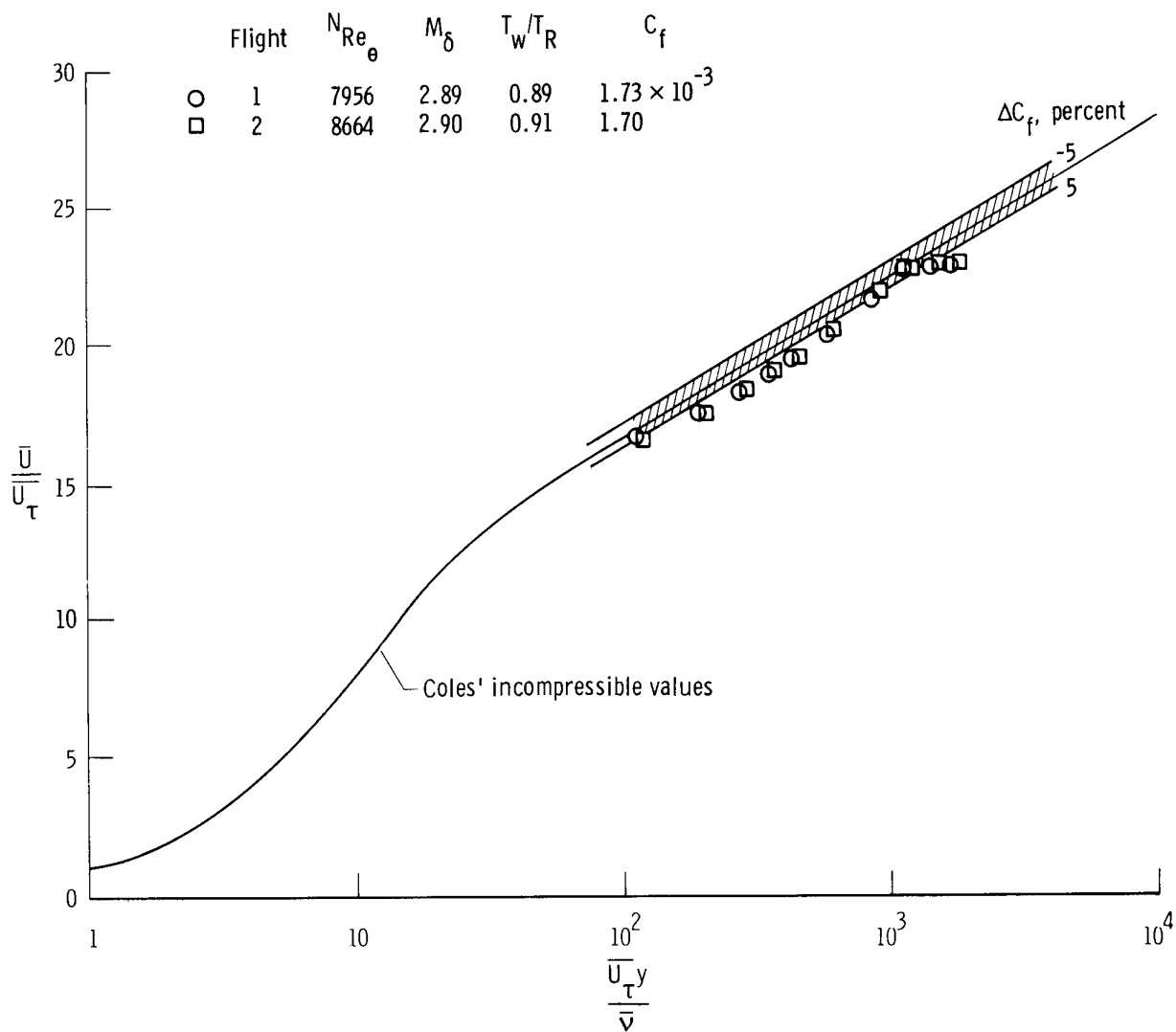
(a) Mixing length transformation of van Driest (ref. 17).

Figure 17. Measured and calculated law-of-the-wall velocity profiles. Measured compressible values transformed to incompressible equivalents using indicated theory.



(b) Eckert's reference enthalpy method (ref. 18).

Figure 17. Continued.



(c) Wall reference temperature method (ref. 19).

Figure 17. Concluded.

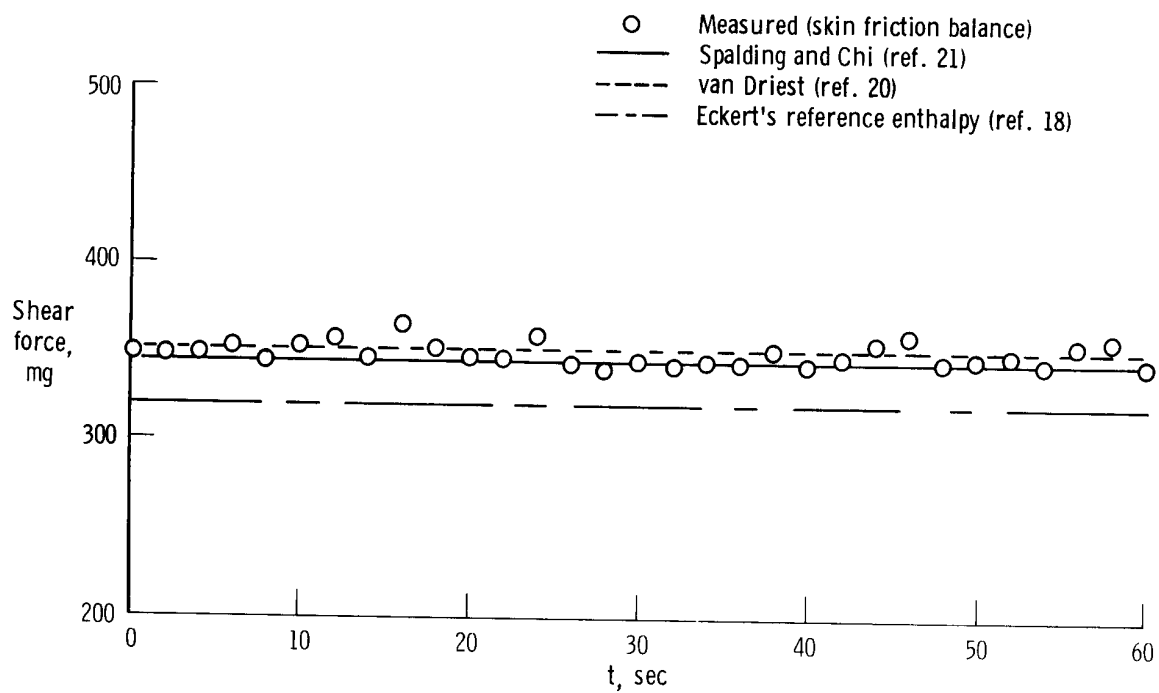
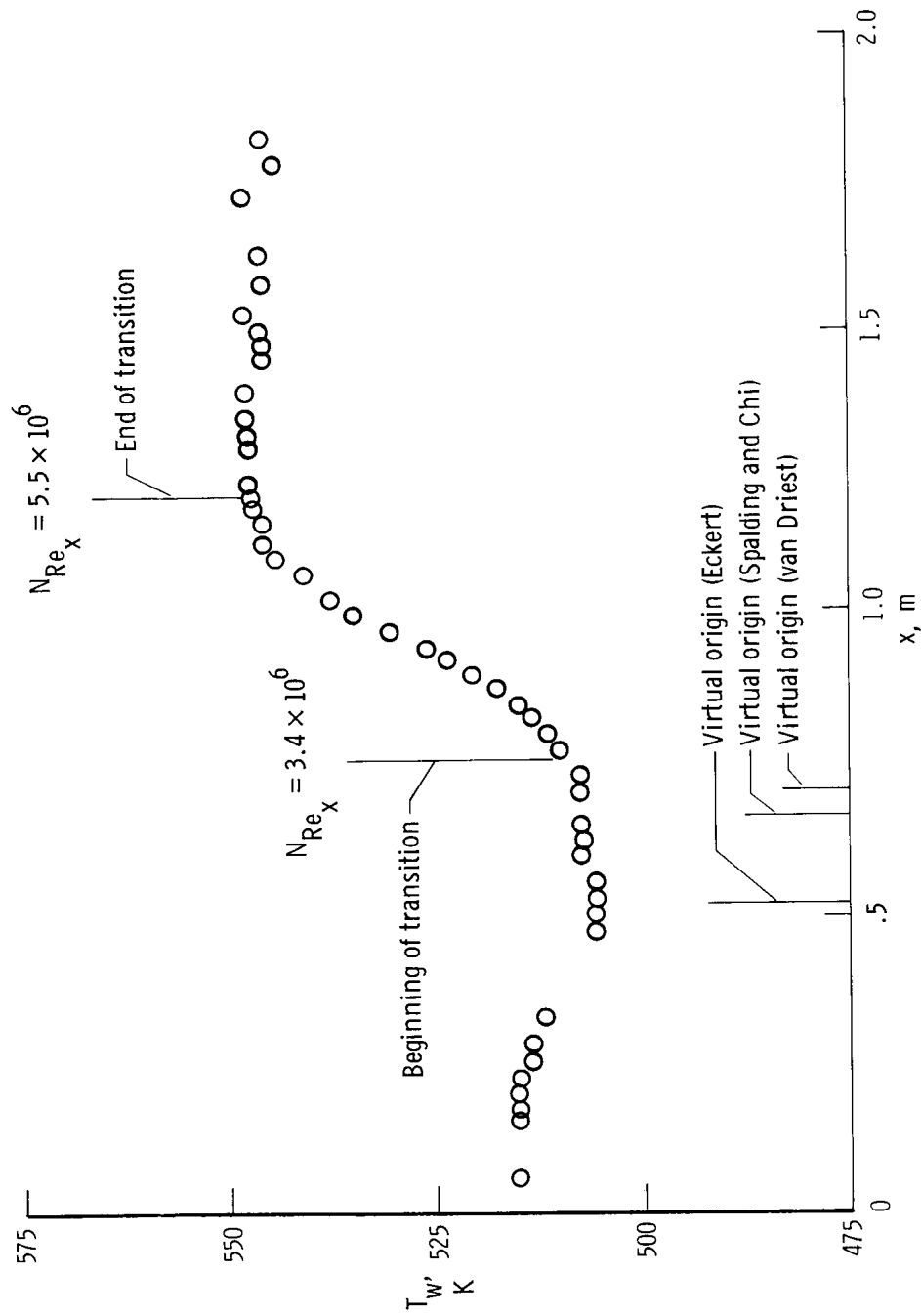
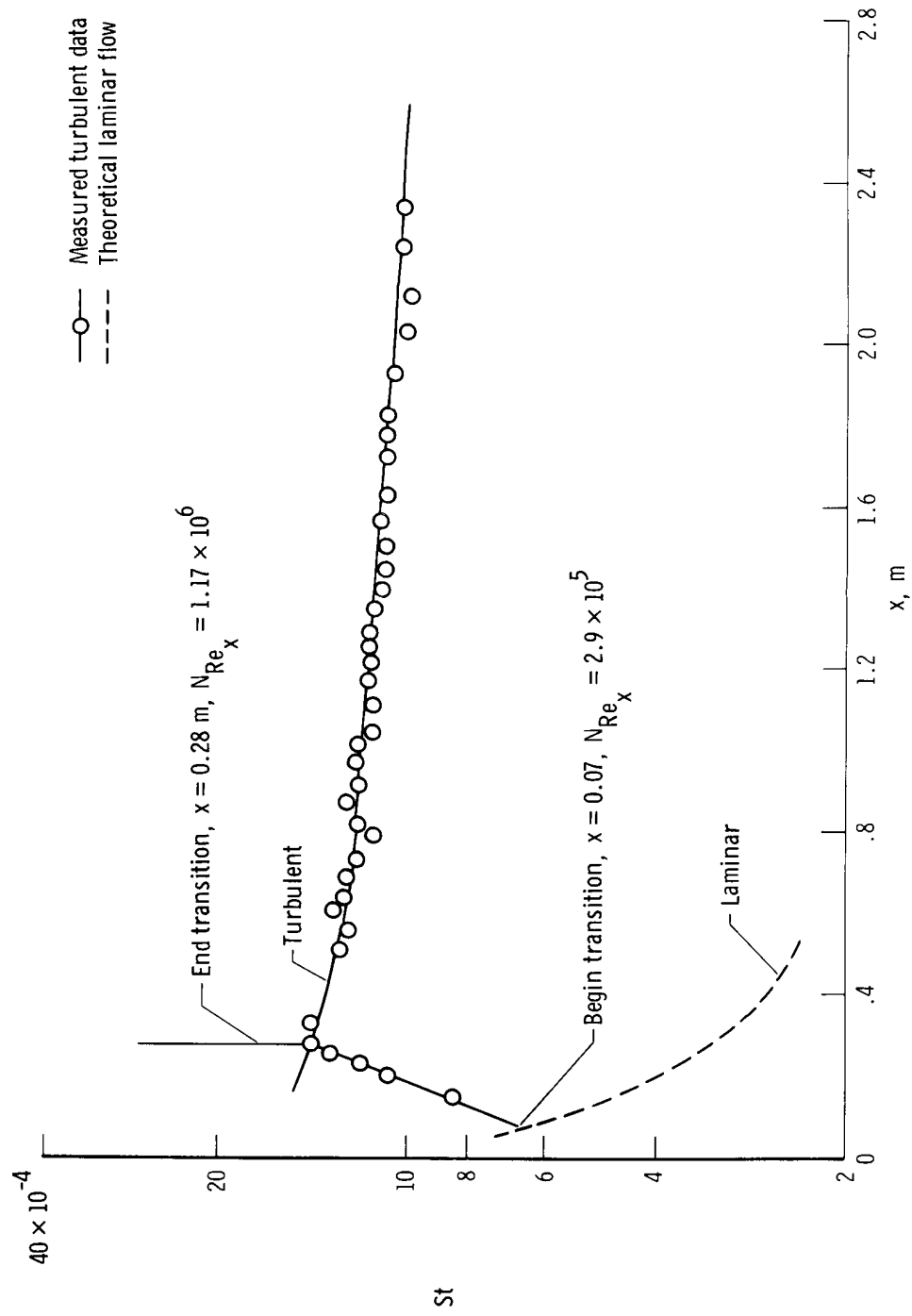


Figure 18. Comparison of measured and calculated skin friction.  $M_\delta = 2.90$ ,  $N_{Re_\theta} = 8664$ ,  $T_w/T_R = 0.91$ . Flight 2.



(a) Flight 2.

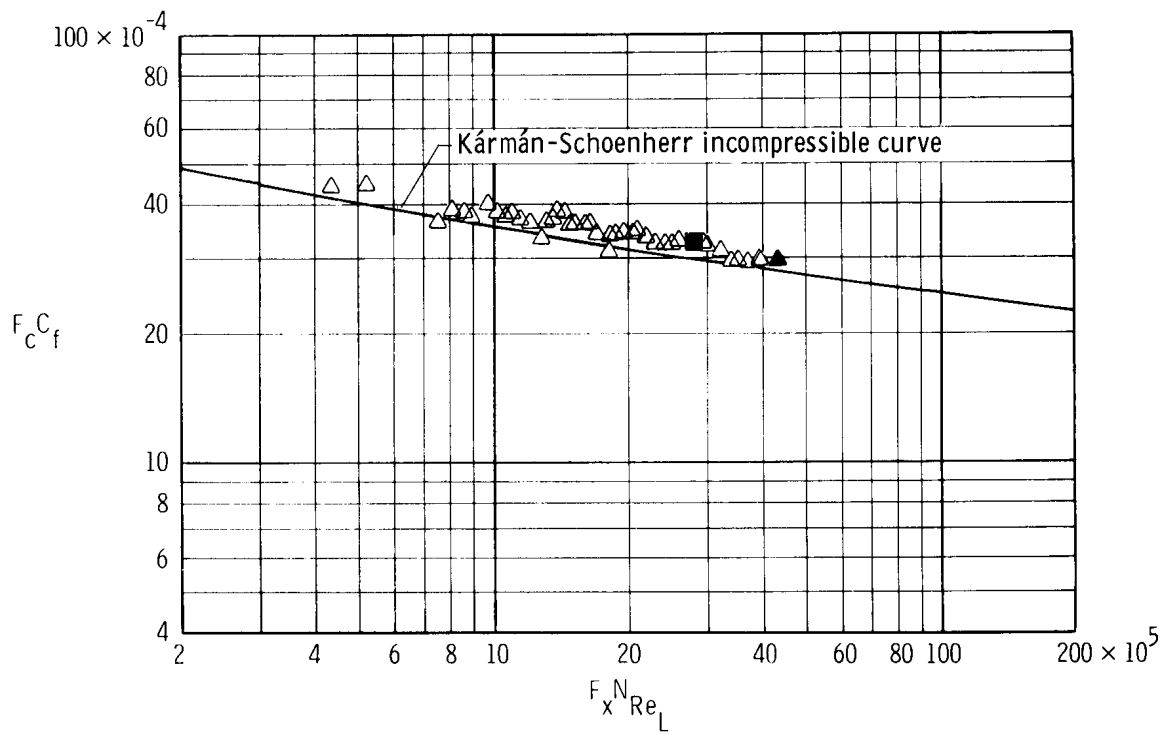
Figure 19. Boundary-layer transition on lower surface.



(b) Flight 3.

Figure 19. Concluded.

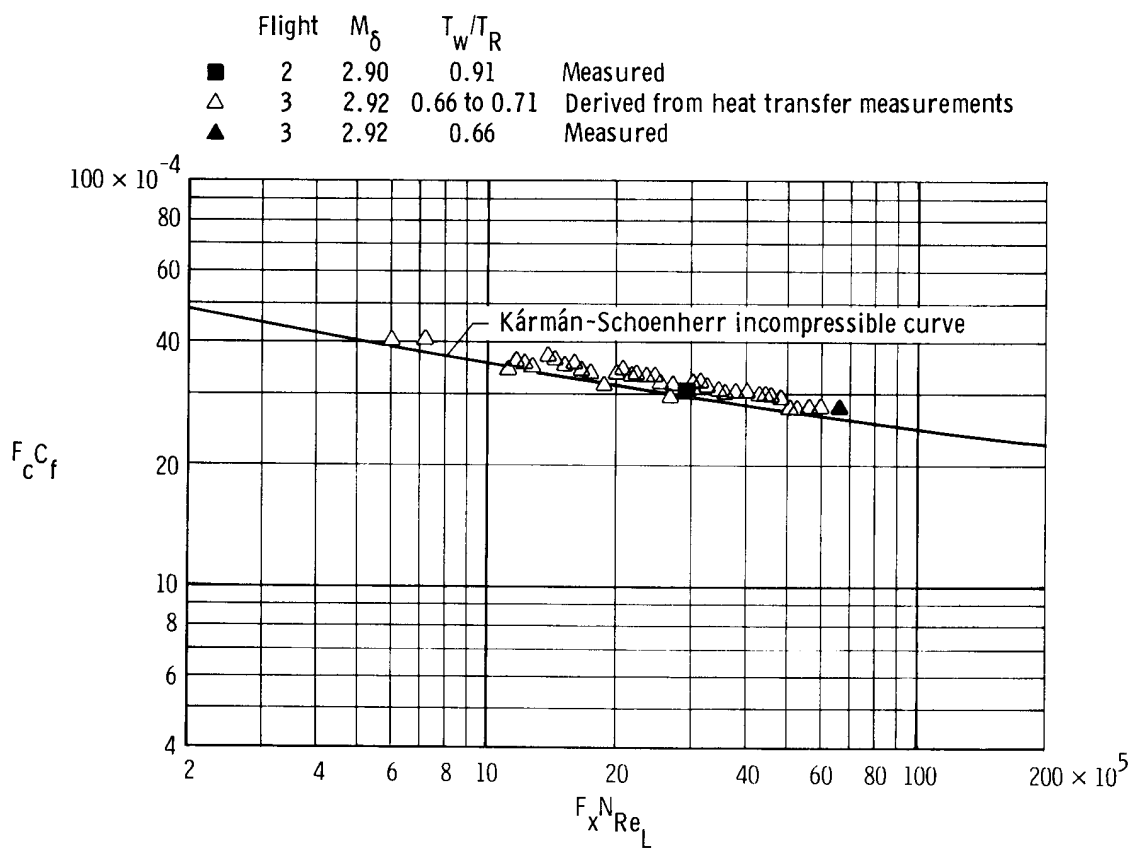
	Flight	$M_\infty$	$T_w/T_R$	
■	2	2.90	0.91	Measured
△	3	2.92	0.66 to 0.71	Derived from heat transfer measurements
▲	3	2.92	0.66	Measured



(a) Eckert's reference enthalpy (ref. 18).

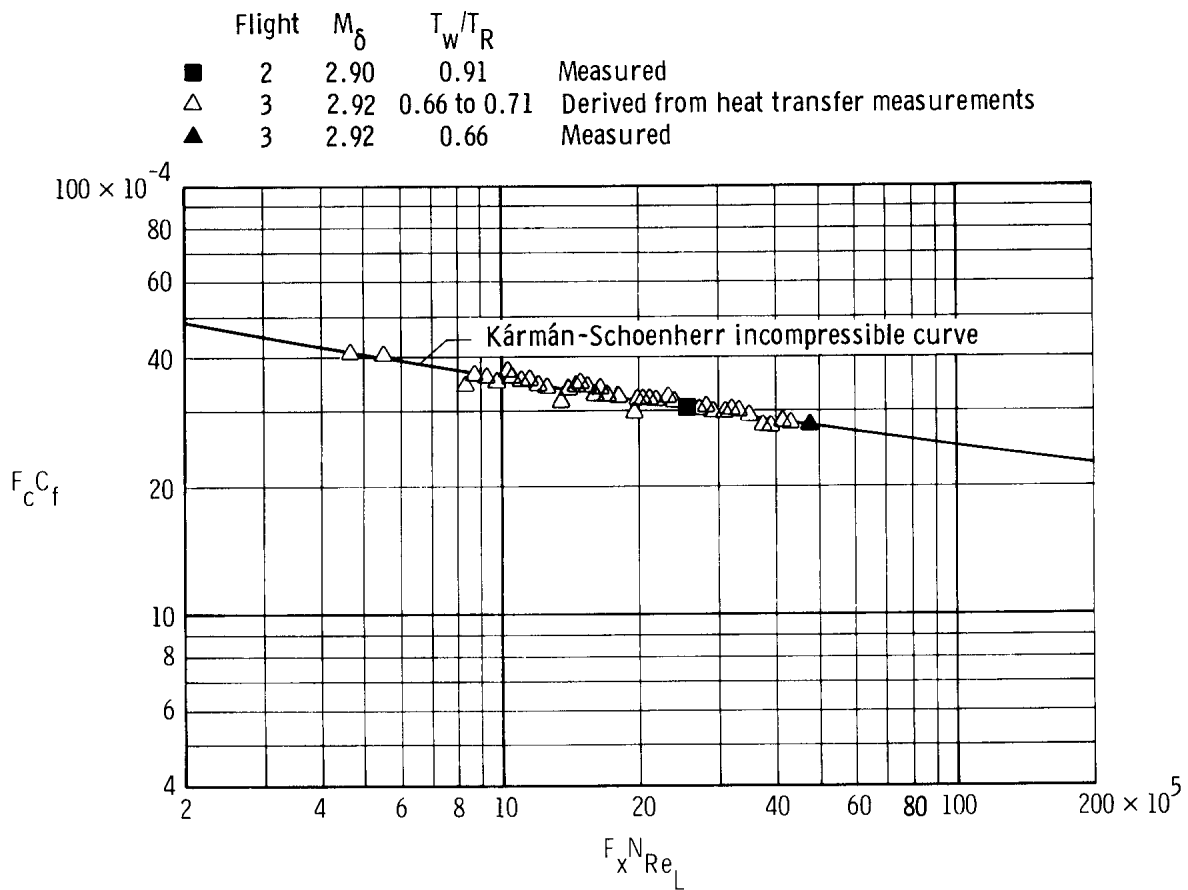
Figure 20. Evaluation of three compressible turbulent skin friction theories.





(b) Spalding and Chi (ref. 21).

Figure 20. Continued.



(c) van Driest (ref. 20).

Figure 20. Concluded.

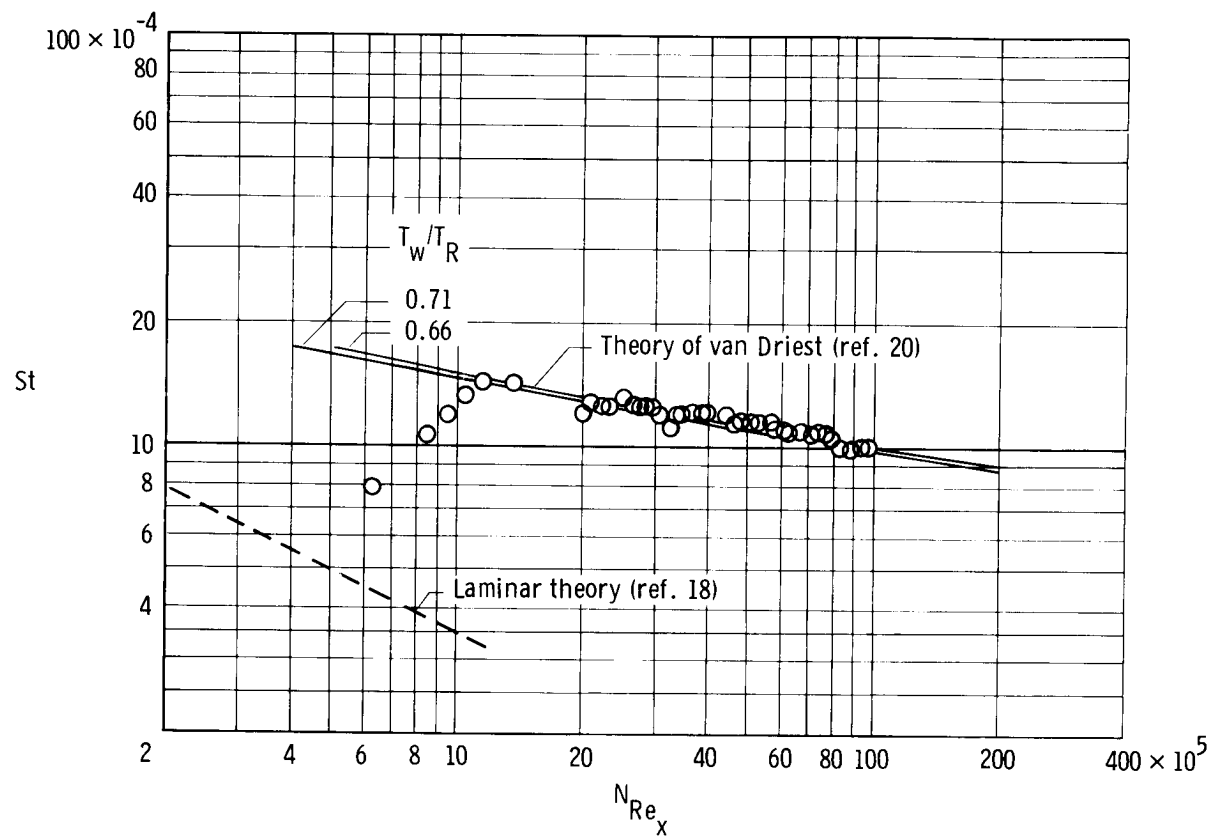


Figure 21. Comparison of measured and calculated heat transfer. Flight 3.

1. Report No. NASA TP-1764		2. Government Accession No.		3. Recipient's Catalog No.	
4. Title and Subtitle IN-FLIGHT BOUNDARY-LAYER MEASUREMENTS ON A HOLLOW CYLINDER AT A MACH NUMBER OF 3.0				5. Report Date November 1980	
				6. Performing Organization Code	
7. Author(s) Robert D. Quinn and Leslie Gong				8. Performing Organization Report No. H-1101	
9. Performing Organization Name and Address NASA Dryden Flight Research Center P.O. Box 273 Edwards, California 93523				10. Work Unit No. 505-43-24	
				11. Contract or Grant No.	
12. Sponsoring Agency Name and Address National Aeronautics and Space Administration Washington, D. C. 20546				13. Type of Report and Period Covered Technical Paper	
				14. Sponsoring Agency Code	
15. Supplementary Notes					
16. Abstract  <p>Skin temperatures, shear forces, surface static pressures, boundary-layer pitot pressures, and boundary-layer total temperatures were measured on the external surface of a hollow cylinder that was 3.04 meters long and 0.437 meter in diameter and was mounted beneath the fuselage of the YF-12A airplane. The data were obtained at a nominal free stream Mach number of 3.0 (a local Mach number of 2.9) and at wall-to-recovery temperature ratios of 0.66 to 0.91. The local Reynolds number had a nominal value of <math>4.3 \times 10^6</math> per meter. Heat transfer coefficients and skin friction coefficients were derived from skin temperature time histories and shear force measurements, respectively. In addition, boundary-layer velocity profiles were derived from pitot pressure measurements, and a Reynolds analogy factor was obtained from the heat transfer and skin friction measurements.</p> <p>The measured data are compared with several turbulent boundary-layer prediction methods.</p>					
17. Key Words (Suggested by Author(s)) Boundary layer Flat plate			18. Distribution Statement Unclassified-Unlimited  Subject category 34		
19. Security Classif. (of this report) Unclassified		20. Security Classif. (of this page) Unclassified		21. No. of Pages 53	
				22. Price* \$7.00	

\*For sale by the National Technical Information Service, Springfield, Virginia 22161

NASA-Langley, 1980